

Effects of Bethe-Heitler pair production in ultraluminous X-ray sources

Gustavo E. Romero^{a,b}, Lucas M. Pasquevich^{a,b}, Leandro Abaroa^{a,b}

^a*Instituto Argentino de Radioastronomía (CCT La Plata, CONICET; CICPBA; UNLP), Cno. Gral. Belgrano, Villa Elisa, 1894, Buenos Aires, Argentina*

^b*Facultad de Ciencias Astronómicas y Geofísicas, Universidad Nacional de La Plata, Paseo del Bosque s/n, La Plata, B1900FWA, Buenos Aires, Argentina*

Abstract

Some black holes in X-ray binaries accrete at rates far above the Eddington limit. In this supercritical regime, photons are trapped in a radiation-dominated, geometrically thick disk. The innermost regions form a complex environment of intense radiation, strong magnetic fields, and powerful outflows, where radiation-driven winds expel large amounts of mass. These conditions suppress primary relativistic electrons within the transparent funnel along the black hole's spin axis. We show that high-energy electrons can instead arise as secondary pairs from Bethe-Heitler interactions between relativistic protons and ambient photons. Using self-similar models of accretion disks with strong winds of ultraluminous X-ray sources (ULXs), we compute particle acceleration via magnetic reconnection and diffusive shocks, evaluate energy losses, and assess the efficiency and spectral imprint of Bethe-Heitler pair production. Our results suggest that secondary pairs can yield nonthermal radiation in the 0.1-100 MeV range with luminosities from 10^{34} up to 10^{38} erg s⁻¹. This emission could be detectable by future MeV instruments from Galactic ULXs, offering evidence of relativistic protons in their inner funnels and revealing misaligned, otherwise hidden, super-Eddington sources in the Milky Way.

Keywords:

Radiation mechanisms: thermal, non-thermal, accretion, accretion disk, stars: winds, outflows, X-ray: binaries, black holes

1. Introduction

A fundamental parameter in the characterization of X-ray binary systems is the accretion rate of matter onto the black hole (BH). Depending on the ratio of the actual accretion rate to the Eddington rate, accretion proceeds in three distinct regimes.

At moderate accretion rates, the system enters the standard disk regime (Shakura and Sunyaev, 1973), characterized by an optically thick, geometrically thin accretion disk.

At very low accretion rates, the inner region of the disk inflates and becomes optically thin. In this case, the accreting gas is advected into the BH before it can cool efficiently, resulting in very high temperatures: approximately $T_e \sim 10^9$ K for electrons and $T_p \sim (m_p/m_e) T_e \sim 10^{12}$ K for protons. This regime, commonly referred to as an advection-dominated accretion flow (ADAF), is described by self-similar solutions developed by Ichimaru (1977) and Narayan and Yi (1994). The ADAF region resembles a hot, two-temperature corona surrounding the BH (e.g., Bisnovatyi-Kogan and Blinnikov, 1976; Liang and Price, 1977). This plasma efficiently Comptonizes the soft radiation from the outer disk, producing hard X-ray emission extending up to photon energies of ~ 150 keV, which is a hallmark of many X-ray binaries.

At the other extreme, when the accretion rate exceeds the Eddington limit, the disk becomes supercritical: geometrically

thick and dominated by radiation pressure in its innermost regions. The luminosity saturates around the Eddington value, while the excess accreting matter is expelled in the form of a strong wind (e.g., Shakura and Sunyaev, 1973; Lipunova, 1999; Fukue, 2004; Ohsuga et al., 2005; Fukue and Iino, 2010; Abaroa et al., 2024; Abaroa and Romero, 2024a). Supercritical accretion is believed to power a variety of energetic astrophysical systems, including microquasars like SS-433, narrow-line Seyfert 1 galaxies, luminous quasars, transient episodes linked to tidal disruption events in supermassive BHs, and ultraluminous X-ray sources (ULXs) observed in external galaxies.

ULXs are believed to be accreting X-ray binaries hosting a compact stellar-mass object, such as a BH, accreting at super-Eddington rates (see Fabrika et al. 2021 for a review). These systems exhibit X-ray fluxes which, if assumed to be isotropic, imply luminosities exceeding $L_X > 10^{39}$ erg s⁻¹ surpassing the Eddington limit for a BH with mass $M_{\text{BH}} \lesssim 10 M_\odot$. The corresponding Eddington luminosity is given by

$$L_{\text{Edd}} = 1.26 \times 10^{38} \left(\frac{M_{\text{BH}}}{M_\odot} \right) \text{ erg s}^{-1}. \quad (1)$$

In such conditions, the accretion rate, \dot{M}_{input} , must exceed the Eddington rate, defined as $\dot{M}_{\text{Edd}} = L_{\text{Edd}}/(\eta_{\text{acc}} c^2)$, where $\eta_{\text{acc}} \sim 0.1$ is the accretion efficiency and c is the speed of light.

The high observed luminosity may also result from geometric beaming (King, 2010): radiation from the inner disk is collimated by a dense, optically thick wind that surrounds the accretion flow, leaving only a narrow, transparent funnel aligned with

Email address: gustavo.esteban.romero@gmail.com (Gustavo E. Romero)

the BH spin axis. As a result, only the innermost regions of the disk contribute to the observed emission, while radiation from the rest of the disk is absorbed and reprocessed by the wind.

However, most ULX spectra in the X-ray band exhibit a combination of a thermal blackbody component and a nonthermal power-law tail (e.g., [Combi et al., 2024](#); [Cruz-Sanchez et al., 2025](#)). The thermal emission is attributed to the hot inner regions of the accretion disk, while the power-law component is generally interpreted as arising from Comptonization of soft photons by relativistic electrons within the magnetocentrifugal funnel, which is confined by the dense wind. Two key open questions remain: how relativistic electrons are accelerated within this funnel, effectively acting as a coronal Comptonizing region in ULXs, and whether relativistic protons are also injected and accelerated in this environment.

Both analytical models and numerical simulations have explored the generation of outflows in supercritical accretion disks (e.g., [Meier, 1979](#); [Eggum et al., 1985](#); [Fukue, 2005](#); [Okuda et al., 2005](#); [Sądowski et al., 2014](#); [McKinney et al., 2015](#); [Sądowski and Narayan, 2015](#); [Sotomayor Checa and Romero, 2019](#); [Kitaki et al., 2021](#); [Abaroa et al., 2023, 2024](#)). These studies show that both strongly magnetized ([McKinney et al., 2015](#)) and nonmagnetized ([Sądowski and Narayan, 2015](#)) disks are capable of launching mildly relativistic outflows in supercritical systems. Accretion of nondipolar magnetic fields and baryon entrainment from clumpy structures ([McKinney and Blandford, 2009](#); [Romero and Gutiérrez, 2020](#)) likely contribute to mass loading at the base of these outflows.

The intense radiation fields near the BH in ULXs are expected to severely limit particle acceleration, especially for relativistic primary electrons, which suffer strong radiative losses that impose a low-energy cutoff in their spectrum. In contrast, protons may be accelerated to significantly higher energies, although not necessarily high enough to efficiently produce photomesons. Nevertheless, Bethe-Heitler ([Bethe and Heitler, 1934](#)) interactions with ambient photons can generate abundant secondary electron-positron pairs. In some cases, these secondary pairs may carry more energy than the primary electrons, and their subsequent inverse Compton (IC) cooling can produce MeV gamma rays that may escape the system, offering a potential observational signature of relativistic protons in the funnel. Moreover, the number of secondary pairs could exceed that of primary electrons by several orders of magnitude, resulting in enhanced nonthermal luminosities in the gamma-ray band. The detectability of this emission depends sensitively on various factors, including the accretion rate and the relative intensity of different photon fields.

In this work, we investigate the role of Bethe-Heitler interactions in ULXs by studying the injection of nonthermal particle populations into the funnels formed by winds in supercritical accretion disks. Our primary objective is to identify observable signatures of proton acceleration in these systems.

The paper is organized as follows. In the next section, we present a self-similar model for supercritical accretion disks with winds and define two representative ULX configurations. We then inject populations of relativistic particles near the BH and estimate the associated energy losses and resulting spec-

tra for both primary electrons and protons within the funnel. In Sect. 4, we compute the production of secondary electron-positron pairs through Bethe-Heitler interactions and analyze their energy evolution. The resulting spectral energy distributions (SEDs) are presented in Sect. 5. In Sect. 6, we examine photon absorption due to the dense wind, particularly at large inclination angles. A discussion of the implications of our results and their potential observational signatures is provided in Sect. 7. We conclude in Sec. 8 with a summary and outlook.

2. Supercritical disks and winds

2.1. General conditions of supercritical disks

When the accretion rate to the BH becomes supercritical, the thin disk approximation breaks down and the disk becomes thick near the compact object (e.g., [Abramowicz et al., 1980](#); [Jaroszynski et al., 1980](#); [Paczynski and Wiita, 1980](#); [Abramowicz et al., 1988](#)). Photons produced well inside the disk are trapped in the flow, that is, the photon diffusion timescale exceeds the accretion timescale (e.g., [Begelman, 1978](#); [Ohsuga et al., 2003, 2005](#); [Kitaki et al., 2021](#)).

The photon trapping effect can be parameterized by considering that the advection heating is a fraction of the viscous heating, $Q_{\text{adv}} = Q_{\text{vis}} - Q_{\text{rad}} = fQ_{\text{vis}}$, where Q_{rad} is the radiative cooling rate and f is the advection parameter, constant along the disk ([Narayan and Yi, 1994](#)). The critical radius of the accretion disk is defined as the distance from the BH where the radiation force overcomes gravity (see [Fukue, 2004](#)):

$$r_{\text{crit}} = \frac{9\sqrt{3}\sigma_{\text{T}}}{16\pi m_{\text{p}}c} \dot{M}_{\text{input}} \approx 40\dot{m}_{\text{input}}r_{\text{g}}, \quad (2)$$

where σ_{T} is the Thomson cross section, $\dot{m}_{\text{input}} = \dot{M}_{\text{input}}/\dot{M}_{\text{Edd}}$ is the normalized accretion rate and $r_{\text{g}} = GM_{\text{BH}}/c^2$ the gravitational radius. If $\dot{M}_{\text{input}} \gg \dot{M}_{\text{Edd}}$, the critical radius can extend to the entire accretion disk, while for $\dot{M}_{\text{input}} \gtrsim \dot{M}_{\text{Edd}}$ there are two different regions in the disk: for $r < r_{\text{crit}}$ the disk is in a supercritical state and for $r > r_{\text{crit}}$ the disk is standard.

In the inner disk there is a strong mass loss of the system in the form of a wind driven by radiation pressure, and the accretion rate is controlled by the Eddington rate. The latter condition implies that the accretion rate for $r < r_{\text{crit}}$ varies as $\dot{M}(r) \propto r$, while it is constant for $r > r_{\text{crit}}$, $\dot{M}(r) = \dot{M}_{\text{input}}$.

Toroidal magnetic fields are expected to develop in the innermost disk of X-ray binaries. There, the overflowing stream from the Roche lobe expands in toroidal and radial directions as it feeds the outer disk. The disk shear should substantially enhance the toroidal component ([Liska et al., 2018](#)). In the innermost region, the energy density of the magnetic field becomes important, so we distinguish an additional part of the accretion disk given by $r_{\text{in}} < r < r_{\text{mag}} (< r_{\text{crit}})$ (see [Akizuki and Fukue, 2006](#)), where r_{mag} is the magnetospheric radius and $r_{\text{in}} = 6r_{\text{g}}$ is the innermost disk radius of a nonrotating BH.

Each region is characterized by a typical temperature. The innermost part has temperatures of $\sim 10^7$ K, the critical region $\sim 10^6$ K, and the standard disk $\sim 10^5$ K. The typical temperature of the ejected wind is a fraction of the temperature of the critical disk.

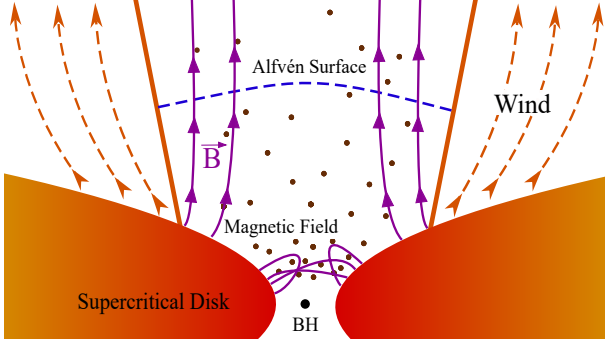


Figure 1: Diagram of the inner region of a ULX system. The dotted region is the funnel formed by the wind around the rotation axis of the BH. Not to scale.

2.2. Disk model

We assume a steady and axisymmetric disk where all physical quantities depend only on the distance to the BH on the equatorial plane, r . The continuity equation for the accreted gas is

$$\frac{1}{r} \frac{d}{dr} (r \Sigma v_r) = 2 \dot{\rho} H, \quad (3)$$

where $\Sigma = \Sigma_0 r^s$ is the surface density (Σ_0 and s are determined later), v_r the radial infall velocity, H the scale height of the disk, and $\dot{\rho}$ the mass loss rate per unit volume.

The radial momentum equation can be written as

$$v_r \frac{dv_r}{dr} - \Omega^2 r = -\Omega_K^2 - \frac{1}{\rho} \frac{d}{dr} (\rho c_s^2), \quad (4)$$

where Ω is the angular velocity, Ω_K the Keplerian angular velocity, and $c_s \equiv \sqrt{p_{\text{gas}}/\rho}$ the isothermal sound speed (p_{gas} is the gas pressure). The angular momentum equation is given by

$$v_r \frac{d}{dr} (\Omega r^2) = \frac{1}{\rho r H} \frac{d}{dr} \left(\frac{\alpha \rho c_s^2 r^3 H}{\Omega_K} \frac{d\Omega}{dr} \right), \quad (5)$$

where we assumed there is no net radial or angular-momentum gain or loss associated with the wind (Fukue, 2004). Here, α is the viscosity parameter.

The final two equations are those of hydrostatic balance in the vertical direction

$$\Omega_K^2 H^2 = c_s^2, \quad (6)$$

and the equation of energy:

$$\frac{\Sigma v_r}{\gamma - 1} \frac{dc_s^2}{dr} + 2H c_s^2 \left(\dot{\rho} - v_r \frac{d\rho}{dr} \right) = f \frac{\alpha \Sigma c_s^2 r^2}{\Omega_K} \left(\frac{d\Omega}{dr} \right)^2, \quad (7)$$

where γ is the ratio of specific heats.

The effects of the magnetic field are neglected in all these equations. To include such effects, Eqs. (4), (5), and (6) should be modified as in Akizuki and Fukue (2006). Additionally, we must introduce the induction equation. For a toroidal magnetic field, the equation is as follows:

$$v_r \frac{dc_A^2}{dr} + c_A^2 \frac{dv_r}{dr} - \frac{c_A^2 v_r}{r} = 2c_A^2 \frac{\dot{B}_\phi}{B_\phi} - c_A^2 \frac{2\dot{\rho} H}{\Sigma}, \quad (8)$$

where $c_A \equiv \sqrt{2p_{\text{mag}}/\rho}$ is the Alfvén speed (p_{mag} is the magnetic pressure).

We solve the dynamic equations of the accreted fluid using the self-similar method of Narayan and Yi (1994). The radial, azimuthal, sound, and Alfvén velocities for radii $r < r_{\text{crit}}$ are given by:

$$v_r(r) = -c_1 \alpha \sqrt{\frac{GM_{\text{BH}}}{r}}, \quad (9)$$

$$v_\phi(r) = c_2 \sqrt{\frac{GM_{\text{BH}}}{r}}, \quad (10)$$

$$c_s^2(r) = c_3 \frac{GM_{\text{BH}}}{r}, \quad (11)$$

$$c_A^2(r) = 2\beta c_3 \frac{GM_{\text{BH}}}{r}, \quad (12)$$

where $\beta = p_{\text{mag}}/p_{\text{gas}}$ is the magnetization.

The coefficients c_1 , c_2 , and c_3 are functions of the model parameters, $c_i = c_i(\alpha, \beta, f, s, \gamma)$. We refer to Fukue (2004) and Akizuki and Fukue (2006) for the functional form of these coefficients.

Using the self-similar solutions, the mass-accretion rate for $r < r_{\text{crit}}$ results

$$\dot{M}(r) = -2\pi r \Sigma v_r = \dot{M}_{\text{input}} \left(\frac{r}{r_{\text{crit}}} \right)^{s+1/2}. \quad (13)$$

The value of the exponent of the self-similar solutions in the critical disk model with mass loss in winds is $s = 1/2$. The toroidal magnetic field is given by (Akizuki and Fukue, 2006):

$$B_\phi = \sqrt{4\pi \Sigma_0 GM_{\text{BH}} \frac{\beta c_3}{\sqrt{(1+\beta)c_3}}} r^{s/2-1}, \quad (14)$$

where $\Sigma_0 = \dot{M}_{\text{input}} r_{\text{mag}} (2\pi c_1 \alpha G^{1/2} M_{\text{BH}}^{1/2} r_{\text{crit}}^2)^{-1}$ (deduced from Eqs. (9) and (13)). Detailed formulae for computing the relevant physical parameters (thickness, temperature, radial velocity, and SED of the radiation emitted) can be found in Fukue (2004) and Akizuki and Fukue (2006).

We compute two different accretion disk scenarios characterized by the parameters given in Table 1 and accretion rates of $10 \dot{M}_{\text{Edd}}$ (scenario A) and $10^3 \dot{M}_{\text{Edd}}$ (scenario B, hyperaccreting source; see e.g., King 2008). We performed Monte Carlo simulations varying the parameters α , β , γ , and f within physically plausible ranges to obtain a set of parameters yielding predicted luminosities with a 95% confidence level, thereby ensuring the robustness of our fiducial disk model.

The magnetospheric radius is estimated as in McKinney et al. (2012) (see also Narayan et al. 2003):

$$r_{\text{mag}} = r_g \left[12000 \left(\frac{3}{4} + \frac{n}{2} \right) \right]^{\frac{4}{3+2n}} \times \epsilon_{-1}^{\frac{2}{3+2n}} m_8^{-\frac{6}{3+2n}} \dot{m}_H^{-\frac{2}{3+2n}} \left(\frac{\Phi}{0.1 \text{ pc}^2 \text{ G}} \right)^{\frac{4}{3+2n}}, \quad (15)$$

where n stands for the relation between the accretion rate $\dot{M}(r)$ and the distance to the BH r (in our case $n = 1$, see Eq. (13)),

$\epsilon_{-1} = \epsilon/0.1$ ($\epsilon \sim 0.01$ relates the advective to the free fall velocity of the plasma in the disk), $m_8 = M_{\text{BH}}/10^8 M_\odot$, $\dot{m}_H \approx 0.15$ is the normalized accretion rate close to the BH (we take the value at the inner radius of the disk, $\dot{m}_H = \dot{m}(r_{\text{in}})$), and Φ is the magnetic flux near the BH (we assume a typical value for X-ray binaries of $\Phi = 10^{-13} \text{ pc}^2 \text{ G}$, see e.g. [Justham et al. 2006](#)). Since the system is supercritical, \dot{m}_H is the same for any value of \dot{M}_{input} . For the parameters assumed in our model, we obtain $r_{\text{mag}} \approx 117 r_g$.

Table 1: Parameters of the accretion disk model.

Parameter	Value (A, B)
BH mass (M_{BH})	$10 M_\odot$
Eddington accretion rate (\dot{M}_{Edd})	$2.2 \times 10^{-7} M_\odot \text{ yr}^{-1}$
Eddington luminosity (L_{Edd})	$1.26 \times 10^{39} \text{ erg s}^{-1}$
Accretion rate (\dot{M}_{input})	$10, 10^3 \dot{M}_{\text{Edd}}$
Gravitational radius (r_g)	$1.5 \times 10^6 \text{ cm}$
Magnetized radius (r_{mag})	$117 r_g$
Critical radius (r_{crit})	$400, 4 \times 10^4 r_g$
Viscosity parameter (α)	0.01
Advection parameter (f)	0.5
Adiabatic index (γ)	4/3
Self-similar exponent (s)	1/2
Magnetization of the inner disk (β)	5

Figure 2 shows on a logarithmic scale the computed properties of the disk for scenarios A (solid blue line) and B (dashed orange line), as a function of r in units of gravitational radius. The disk's thickness (top left) increases with r up to a maximum at r_{crit} , where it rapidly decays to the standard constant value. The radial velocity (top right) approaches a value of approximately $0.1c$ near the BH in both scenarios. Temperatures (bottom left) in the inner region can be as high as $T \sim 10^7 \text{ K}$, dropping below $T \sim 10^5 \text{ K}$ beyond the critical radius. The magnetic field in the inner region can be very high close to the BH, with an order-of-magnitude difference between the two scenarios: $5 \times 10^7 \text{ G}$ (A) and $5 \times 10^6 \text{ G}$ (B). Note that the equations for the scale height and radial velocity are modified with softening factors at r_{mag} and r_{crit} , where the disk's physical parameters change abruptly.

Figure 3 shows the SEDs of the disks without considering either the wind absorption or the geometrical beaming. In both scenarios, the intrinsic luminosity in the X-ray band is $\sim 10^{39} \text{ erg s}^{-1}$, that is, limited to the Eddington luminosity for the assumed BH mass. The disk SEDs, considering both absorption and beaming, are presented in Sect. 5 along with all the radiative processes of the system.

Unlike optically thin and very hot ADAFs, supercritical sources are not hot enough for efficient Comptonization. If Comptonization does occur, it must be produced by an additional component, such as a corona. However, the existence of a stable corona in super-Eddington sources is questionable, as radiation pressure blows away any plasma above the disk. The model of this ejected plasma is described below.

2.3. Wind of the disk

We assume that the wind ejected in radii $r < r_{\text{crit}}$ is highly ionized and blows off at a constant speed ($\beta_w = v_w/c$) and with a constant mass-outflow rate ($\dot{m}_w = \dot{M}_w/\dot{M}_{\text{Edd}}$). Since the disk self-regulates the luminosity approximately at the Eddington value, almost all the accreted mass is removed from the system through the wind (i.e., $\dot{m}_w \approx \dot{m}_{\text{input}}$). Its terminal speed can be estimated as $v_w = c/\sqrt{40 \dot{m}_{\text{input}}}$ ([King, 2010](#)). We get velocities of $0.05c$ and $0.005c$ for scenarios A and B, respectively. Therefore, $\beta_w \ll 1$ and $\gamma_w \approx 1$, so the comoving properties of the wind are essentially equal to those observed. We assume that the wind is spherically symmetric, except for a narrow funnel around the BH axis, a common assumption for ULXs.

The wind mass-loss rate is much higher than the Eddington accretion rate onto the BH, so the wind is optically thick and emits blackbody radiation. The temperature T_w is given by (see e.g., [Abaroa and Romero, 2024b](#))

$$\sigma_T T_w^4 = \dot{e} \frac{L_{\text{Edd}}}{4\pi R^2}, \quad (16)$$

where $\dot{e} \sim 0.1$ is the luminosity in Eddington units and $R = \sqrt{r^2 + z^2}$. Figure 4 shows the SEDs of winds corresponding to cases A and B. The maximum luminosities are $\lesssim 10^{38} \text{ erg s}^{-1}$. The wind photospheres are located at $\sim 2 \times 10^3 r_g$ (A) and $\sim 2 \times 10^6 r_g$ (B), with temperatures $\sim 10^5 \text{ K}$ (A) and $\sim 10^4 \text{ K}$ (B).

We describe next the funnel formed by the wind walls along the spin axis of the BH and the particle gas flowing through it.

2.4. Gas in the funnel

We assume that a gas of particles travels at semi-relativistic speeds through the transparent channel formed by the conical wind above the BH. These particles can enter the funnel directly from the innermost disk, where magnetic reconnection and accretion of non-dipolar magnetic fields can produce rapid flares that drag the particles along (see [Romero and Gutiérrez 2020](#)).

In ULXs, the gas density must be low enough to ensure the funnel is optically thin – an observer at infinity must be able to see the radiation from the innermost accretion disk, so the optical depth must satisfy $\tau < 1$. The density of the gas in the funnel is given by $\rho_{\text{gas}} = \dot{M}_{\text{gas}}/\Omega z^2 v_{\text{gas}}$, where \dot{M}_{gas} is the mass input to the funnel, $\Omega = 2\pi(1 - \cos \vartheta)$ is the solid angle of the duct, and z is the height above the BH. The semi-opening angle of the funnel ϑ is related, in principle, to the accretion mass-rate \dot{m}_{input} ([King, 2010](#)). We assumed semi-opening angles of $\vartheta_A = 15^\circ$ (see e.g., [Veledina et al. 2024](#)) and $\vartheta_B = 5^\circ$ (the higher the mass loss in winds, the narrower the funnel), and the same gas velocity for both scenarios, $v_{\text{gas}} = 0.2c$ ([Pinto et al., 2016](#); [Kosec et al., 2018](#); [Fabrika et al., 2021](#); [Abaroa et al., 2023](#)).

We then solve the integral for the optical depth inside the funnel:

$$\tau = \int_0^\infty \gamma_{\text{gas}}(1 - \beta_{\text{gas}} \cos \vartheta) \kappa_{\text{co}} \rho_{\text{co}} dz = 1, \quad (17)$$

where $\rho_{\text{co}} \approx \rho_{\text{gas}}$ and $\kappa_{\text{co}} \approx \kappa = \sigma_T/m_p$ is the opacity, with σ_T the Thomson scattering and m_p the proton mass. We thus obtain

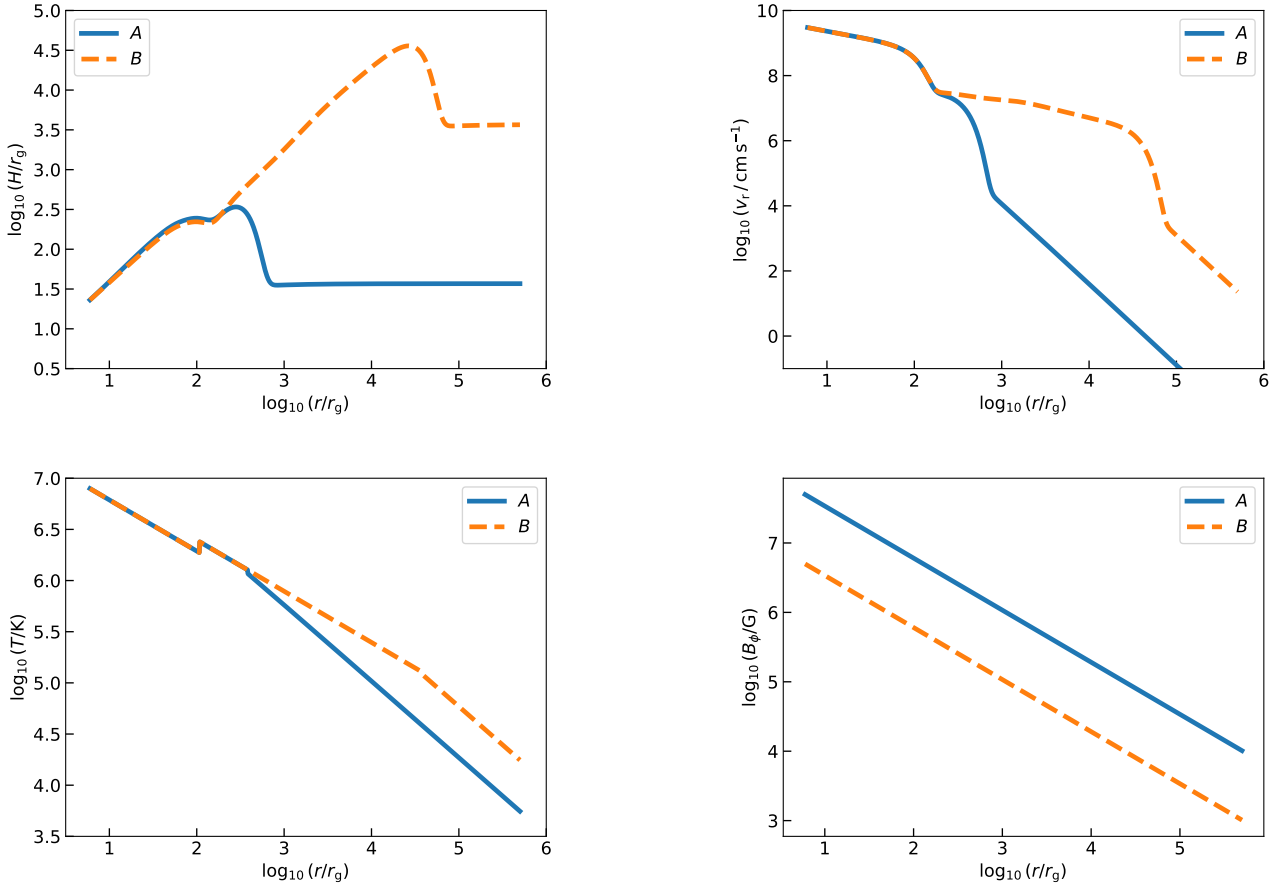


Figure 2: Radial distribution of the thickness (top left), radial velocity (top right), temperature (bottom left), and toroidal magnetic field (bottom right) of the accretion disk. Thickness and radial distance to the BH are in units of gravitational radius. Radial velocity and magnetic field are in CGS units. The magnetospheric radius is at $\sim 117 r_g$, while the critical radius is at $\sim 400 r_g$ (A) and $\sim 40000 r_g$ (B). We show results for scenarios A ($\dot{m}_{\text{input}} = 10$, solid blue lines) and B ($\dot{m}_{\text{input}} = 10^3$, dashed orange lines).

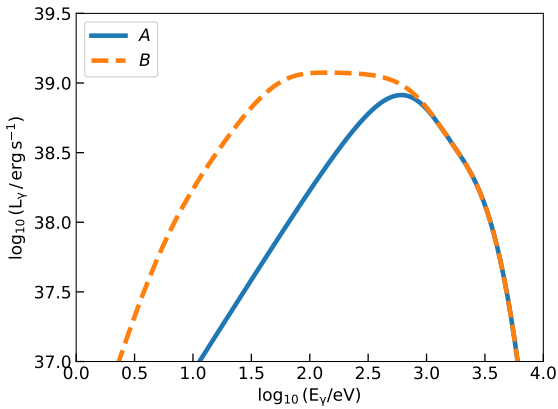


Figure 3: Unabsorbed and unbeamed thermal SEDs of the supercritical magnetized accretion disk for scenarios A ($\dot{m}_{\text{input}} = 10$, solid blue line) and B ($\dot{m}_{\text{input}} = 10^3$, dashed orange line). The maximum luminosity is limited to the Eddington luminosity, $\sim 10^{39} \text{ erg s}^{-1}$.

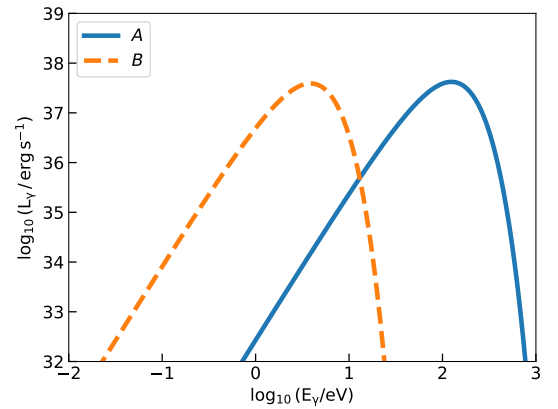


Figure 4: SEDs of the disk-driven wind for scenarios A (solid blue line) and B (dashed orange line). The luminosity in both cases is a fraction $\dot{e} \sim 0.1$ of the Eddington luminosity.

the condition $\rho_{\text{gas}} < 5 \times 10^{-11} \text{ g cm}^{-3}$ with the parameters of our model for both scenarios. We assume this value for the gas den-

sity to calculate the radiative processes inside the funnel in two scenarios considered. We note that, since this is the maximum density allowed, the different results that we will obtain should be considered as upper limits.

3. Relativistic primary particles

We assume that there is a region of efficient particle acceleration inside the funnel and evaluate two possible mechanisms: diffusive shock acceleration (scenarios A_1 and B_1) and magnetic reconnection (scenarios A_2 and B_2). If shocks mediate the acceleration mechanism, then the region must be located at a distance such that the kinetic energy of the gas exceeds its magnetic energy; otherwise, the fluid would be mechanically incompressible. On the other hand, magnetic reconnection should occur near the BH, in order for the magnetic field to be sufficiently large.

Internal shocks caused by differential bulk motions occur when the matter-energy density is greater than the magnetic energy density, $e_p(z) = \dot{M}_{\text{gas}} v_{\text{gas}} / 2\pi z^2 > B^2(z) / 8\pi = e_m(z)$. The strength of the magnetic field near the BH was calculated in Sect. 2.2. Its value for the two scenarios is $B(A_1) \sim 5 \times 10^7$ G and $B(B_1) \sim 5 \times 10^6$ G, and decays as $\propto z^{-2}$ above the BH up to the Alfvén radius. We find that $e_p(z) > e_m(z)$ at heights $z_{\text{acc}}(A_1) \sim 200 r_g$ and $z_{\text{acc}}(B_1) \sim 60 r_g$. We assume that the acceleration region is at $2000 r_g$ (A_1) and $100 r_g$ (B_1), where the magnetic fields are $B(A_1) \approx 10^4$ G and $B(B_1) \approx 8 \times 10^4$ G. The size of the acceleration region in both cases is $\Delta z_{\text{acc}} = 0.1 z_{\text{acc}}$.

The specific mechanism by which baryons are injected into the funnel remains uncertain, although several possibilities are discussed by, e.g., [Romero and Gutiérrez \(2020\)](#). The physical conditions inside do not change significantly, so it can be considered as homogeneous. Basic parameters of this one-zone injector are given in Table 2.

In the region $z_{\text{acc}} \leq z \leq z_{\text{max}} = z_{\text{acc}} + \Delta z_{\text{acc}}$ a small fraction of the total power L (see Sect. 2.4) is transferred to relativistic particles:

$$L_{\text{rel}} = q_{\text{rel}} L, \quad (18)$$

where we adopt $q_{\text{rel}} = 0.1$ and L_{rel} as the total power injected into both relativistic protons and electrons:

$$L_{\text{rel}} = L_p + L_e. \quad (19)$$

In addition, we assume that the mechanism is more efficient for protons, with a composition $a \sim m_p/m_e \approx 10^3$:

$$L_p = a L_e. \quad (20)$$

The kinetic power of the outflow,

$$L_{\text{gas}} = \frac{\dot{M}_{\text{gas}} v_{\text{gas}}^2}{2}, \quad (21)$$

is $10^{36} \text{ erg s}^{-1}$ for scenario A_1 and $10^{35} \text{ erg s}^{-1}$ for scenario B_1 . On the other hand, the power carried by the magnetic field is ([del Valle et al., 2011](#)):

$$L_{\text{mag}} = \frac{B^2 A(r) v_a}{8\pi}. \quad (22)$$

Here, $A(r) \approx 4\pi r_{\text{acc}}^2$ is the surface area of the reconnection zone, and $v_a = \sqrt{B^2 / (4\pi m_p n)}$ is the Alfvén speed ($\sim c$). The resulting magnetic power is $5 \times 10^{38} \text{ erg s}^{-1}$ for scenario A_2 and $6 \times 10^{35} \text{ erg s}^{-1}$ for scenario B_2 .

The expected injection function is a power-law in the energy of the primary particles

$$Q(E) = Q_0 E^{-p}, \quad [Q] = \text{erg}^{-1} \text{s}^{-1} \text{cm}^{-3}, \quad (23)$$

where $p = 2$ for scenarios A_1 and B_1 .

In the magnetically-dominated regime, the injection spectral index depends on the magnetization of the system (σ_{mag}):

$$\sigma_{\text{mag}} = \frac{B^2}{4\pi m n c^2 w_n} > 1, \quad (24)$$

where B is the magnetic field, n is the total particle number density, and $w_n = \gamma + P/(m n c^2)$ is the enthalpy per particle. For a cold gas $w_n \sim 1$, so $\sigma_{\text{mag}} = B^2 / (4\pi m n c^2)$.

For slightly magnetized systems ($\sigma_{\text{mag}} \gtrsim 1$) the injection is $p \approx 4$; for moderate magnetization ($\sigma_{\text{mag}} \approx 10$) the index is $p \approx 2$, while in highly magnetized systems, the spectral index can be as hard as $p \sim 1.5$ ([Kagan et al., 2015](#)). With $\rho_{A_2} = 0.1 \rho_{\text{max}, A_2}$ and $\rho_{B_2} = 0.001 \rho_{\text{max}, B_2}$, we get $\sigma_{\text{mag}} \approx 10$.

The normalization constant Q_0 is obtained from

$$L_{(e,p)} = \int_V d^3r \int_{E_{(e,p)}^{\min}}^{E_{(e,p)}^{\max}} dE_{(e,p)} E_{(e,p)} Q_{(e,p)}(E_{(e,p)}), \quad (25)$$

where V is the volume of the acceleration region. The maximum energy E^{max} that a relativistic particle can attain results from balancing its acceleration rate with the cooling or escape rate.

The acceleration rate for a charged particle in a magnetic field B is (see [Drury, 1983](#); [Aharonian, 2004](#)):

$$t_{\text{acc}}^{-1} = \frac{\eta e c B}{E}, \quad (26)$$

where E is the energy of the particle and η is a parameter that characterizes the efficiency of the acceleration mechanism. In the case of diffusive shocks, we typically assume an efficiency of 10^{-2} , while in the case of magnetic reconnection, the efficiency is ([Drury, 1983](#); [del Valle et al., 2011](#); [Vieyro and Romero, 2012](#)):

$$\eta_{\text{mag}} \sim 0.1 \frac{r_{\text{gc}}}{D(E)} \left(\frac{v_{\text{rec}}}{c} \right)^2, \quad (27)$$

where the diffusion coefficient in the Bohm regime is $D(E) = r_{\text{gy}} c / 3$, and $r_{\text{gy}} = E / (eB)$ is the gyroradius of the particle. In violent reconnection events, the reconnection speed approaches the Alfvén speed, i.e., $v_{\text{rec}} \sim v_a$. Since $v_a \sim c$ in our scenario, the resulting acceleration efficiency is $\eta_{\text{mag}} = 0.3$.

The cooling rate of the particles is equal to the sum of their radiative and adiabatic cooling rates:

$$t_{\text{cool}}^{-1} = t_{\text{rad}}^{-1} + t_{\text{ad}}^{-1}. \quad (28)$$

We consider electron losses due to synchrotron radiation, IC scattering, and relativistic Bremsstrahlung, and proton losses

Table 2: Characteristic parameters of the particle acceleration region for models A_1 , B_1 , A_2 and B_2 .

Parameter	Symbol	Value (A_1)	Value (B_1)	Value (A_2)	Value (B_2)	Unit
Height above the disk	z_{acc}	2000	100	10	10	r_g
Radius	r_{acc}	535	9	2.6	0.8	r_g
Size of acceleration region	Δz_{acc}	200	10	1	1	r_g
Thermal particle density	n_{gas}	3.2×10^{12}	1.3×10^{15}	1.3×10^{16}	1.3×10^{14}	cm^{-3}
Magnetic field	$B(z_{\text{acc}})$	10^4	8×10^4	5×10^7	5×10^6	G
Height of the wind photosphere	H_{ph}	1900	2×10^6	1900	2×10^6	r_g
Half-opening angle of the funnel	ϑ	15	5	15	5	degree
Shock velocity	v_s	0.3	0.3			c
Particle acceleration efficiency	η	10^{-2}	10^{-2}	0.3	0.3	
Fraction of power transferred to relativistic particles	q_{rel}	0.1	0.1	0.1	0.1	
Proton to electron ratio	a	10^3	10^3	10^3	10^3	
Index of the power law of injected particles	p	2	2	2	2	

resulting from synchrotron radiation, inelastic proton-proton collisions (pp), and photon-proton interactions ($p\gamma$). These losses are calculated using standard formulae given by [Blumenthal and Gould \(1970\)](#); [Begelman et al. \(1990\)](#); [Kelner et al. \(2006\)](#); [Kelner and Aharonian \(2008\)](#); [Romero and Vila \(2008\)](#).

The adiabatic losses are caused by the expansion of the gas ([Bosch-Ramon et al., 2006](#)),

$$t_{\text{ad}}^{-1} = \frac{2}{3} \frac{v_{\text{gas}}}{z}. \quad (29)$$

The size of the acceleration region may be a constraint on the maximum energy if the particle gyroradius is greater than the linear size of such region (Hillas criterion).

In the "one-zone" approximation, the stationary particle distribution $N(E)$ can be obtained as the solution to the transport equation (e.g., [Ginzburg and Syrovatskii, 1964](#); [Berezinskii et al., 1990](#)):

$$\frac{\partial}{\partial E} \left[\frac{dE}{dt} \Big|_{\text{loss}} N(E) \right] + \frac{N(E, z)}{t_{\text{esc}}} = Q(E), \quad (30)$$

where $t_{\text{esc}} \approx \Delta z_{\text{acc}}/v_{\text{gas}}$ is the particle escape time from the acceleration region in scenarios A_1 and B_1 . In contrast, in scenarios A_2 and B_2 , where particles are magnetically confined, the dominant escape mechanism is diffusion, characterized by the rate $t_{\text{diff}}^{-1} = 2D(E)/r_{\text{acc}}^2$, where $D(E)$ is the diffusion coefficient (we assume Bohm diffusion).

The exact solution to Eq. (30) is given by (see [Khangulyan et al., 2007](#)):

$$N(E) = \left| \frac{dE}{dt} \Big|_{\text{loss}}^{-1} \int_E^{E_{\text{max}}} dE' Q(E') \exp\left(-\frac{\tau(E, E')}{t_{\text{esc}}}\right), \quad (31)$$

where

$$\tau(E, E') = \int_E^{E'} dE'' \left| \frac{dE''}{dt} \Big|_{\text{loss}}^{-1}. \quad (32)$$

Figure 5 shows the cooling and energy gains of primary electrons in the acceleration region for different scenarios. The maximum energies obtained are ~ 80 GeV (A_1), ~ 5 GeV (B_1), ~ 5 GeV (A_2), and ~ 10 GeV (B_2). As expected, IC scattering of thermal photons from the disk and synchrotron radiation are

the dominant losses. Bremsstrahlung, on the other hand, is negligible in all cases because of the low matter density inside the funnel.

Figure 6 shows the cooling and energy gain rates for protons. Because of the intense radiation fields, the dominant radiative cooling mechanism is photo-hadronic interaction, as expected. In scenarios A_1 and B_1 , particle escape is the dominant process. Photomeson production is only relevant in a narrow energy range near the maximum proton energy of ~ 10 TeV. In contrast, proximity to the disk in scenarios A_2 and B_2 results in stronger radiation and magnetic fields in the acceleration region. In these scenarios, radiative losses dominate, and photo-hadronic interactions are the primary cooling channel at energies above ~ 100 GeV. The maximum proton energies achieved are ~ 5 PeV for A_2 and ~ 200 TeV for B_2 . Because of the low density, proton-proton losses are negligible in all scenarios. As shown in the figure, the production of electron-positron pairs via the Bethe-Heitler ($p\gamma$ B-H) mechanism is significant in all cases. We will focus on this mechanism in the next section.

4. The Bethe-Heitler secondary pair injection

Primary electrons cool via synchrotron and IC radiation. The main interaction process for protons in the funnel involves proton-photon ($p\gamma$) collisions. This interaction has two main channels. The first is the Bethe-Heitler effect, also known as photo-pair production

$$p + \gamma \rightarrow p + e^- + e^+, \quad (33)$$

with a threshold energy of ~ 1 MeV for the photon in the proton rest frame.

The second channel is photomeson production, which proceeds through two main branches:

$$p + \gamma \rightarrow p + a\pi^0 + b(\pi^+ + \pi^-), \quad (34)$$

and

$$p + \gamma \rightarrow n + \pi^+ + a\pi^0 + b(\pi^+ + \pi^-), \quad (35)$$

with approximately the same cross-section and a threshold energy of ~ 145 MeV. Here, a and b are the pion multiplicities.

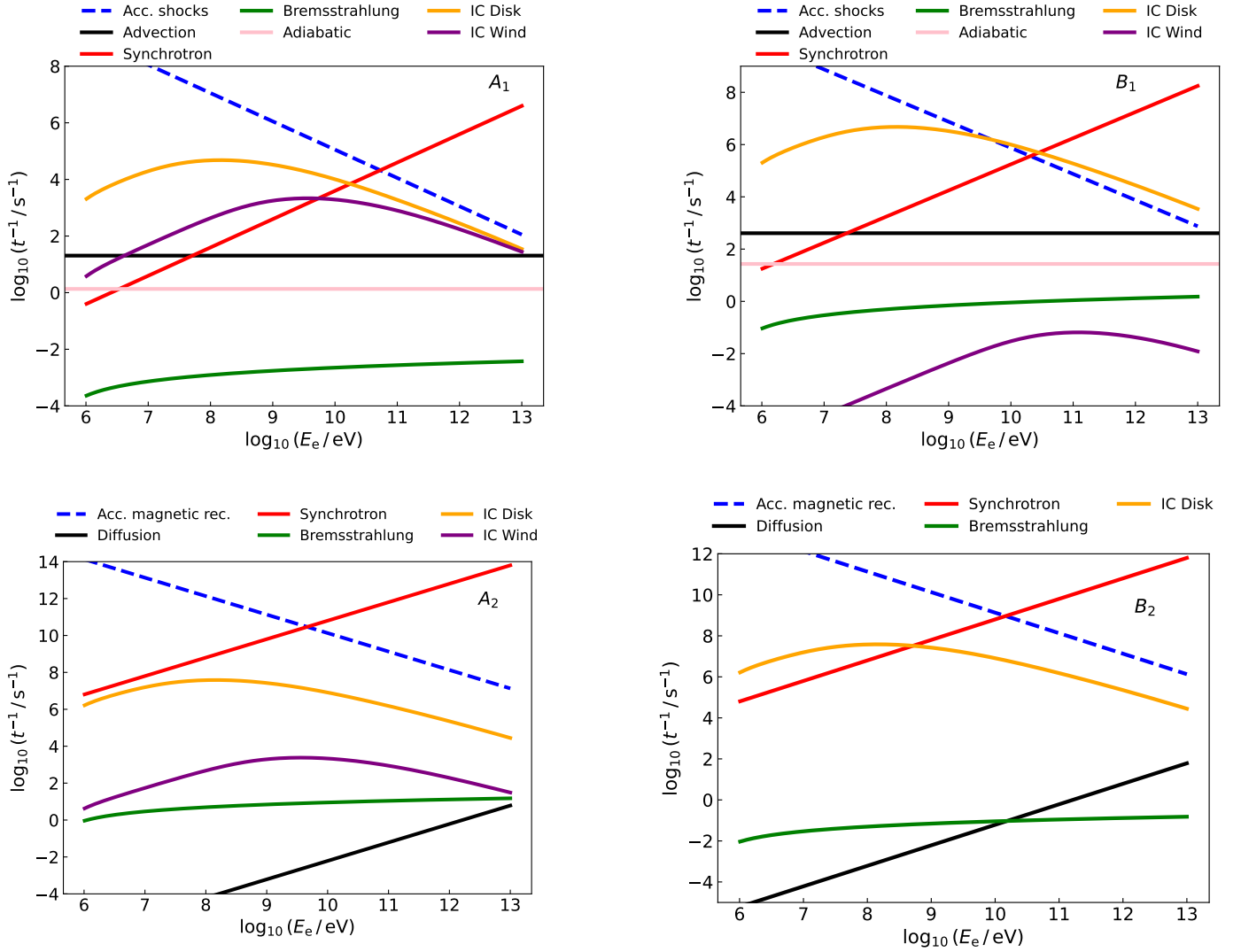


Figure 5: Timescales for the acceleration, cooling, and escape of relativistic electrons. **Top left:** Electron rates for $\dot{m} = 10$ at $z = 2000 r_g$ (A_1), where the acceleration mechanism is diffusive shock acceleration. The dominant cooling process is IC at low energies and synchrotron radiation at higher energies. The maximum electron energy is ~ 50 GeV. **Top right:** Electron rates for $\dot{m} = 1000$ at $z = 200 r_g$ (B_1), with diffusive shocks as the acceleration mechanism. IC losses dominate across the entire energy range. The maximum energy is ~ 6 GeV. **Bottom left:** Electron rates for $\dot{m} = 10$ at $z = 10 r_g$ (A_2). The acceleration mechanism is magnetic reconnection. Synchrotron radiation dominates the cooling, with a maximum energy of ~ 3 GeV. **Bottom right:** Electron rates for $\dot{m} = 1000$ at $z = 200 r_g$ (B_2). The acceleration mechanism is magnetic reconnection. IC cooling dominates up to ~ 1 GeV, after which synchrotron losses dominate. The maximum energy reached is ~ 20 GeV.

Charged pions decay in leptons and neutrinos,

$$\pi^+ \rightarrow \mu^+ + \nu_\mu, \quad \mu^+ \rightarrow e^+ + \nu_e + \bar{\nu}_\mu \quad (36)$$

$$\pi^- \rightarrow \mu^- + \bar{\nu}_\mu, \quad \mu^- \rightarrow e^- + \bar{\nu}_e + \nu_\mu, \quad (37)$$

whereas neutral pion decay yields photons: $\pi^0 \rightarrow 2\gamma$.

In this paper, we are mainly interested in the secondary pairs injected via the Bethe-Heitler mechanism. This process has been studied, for example, by Chodorowski et al. (1992), Mücke et al. (2000), and Mastichiadis et al. (2005). The emissivity of pairs in the δ -functional approximation is calculated as in Romero and Vila (2008). The inelasticity can be approximated by its value at the threshold, $K_{py,e^\pm} = 2m_e/m_p$. Therefore

we have,

$$\begin{aligned} Q_{e^\pm}(E_{e^\pm}) &= 2 \int dE_p N_p(E_p) \omega_{py,e^\pm}(E_p) \delta\left(E_{e^\pm} - \frac{m_e}{m_p} E_p\right) \\ &= 2 \frac{m_p}{m_e} N_p\left(\frac{m_p}{m_e} E_{e^\pm}\right) \omega_{py,e^\pm}\left(\frac{m_p}{m_e} E_{e^\pm}\right). \end{aligned} \quad (38)$$

An useful parametrization of the cross section σ_{py,e^\pm} can be found in Maximon (1968). Since the outflow is not relativistic ($\gamma_{\text{gas}} \approx 1$), the above expressions are the same for both the co-moving and observer reference frames. We calculate the emissivity of electron-positron pairs injected into the same region as the primary particles, using the same ambient fields.

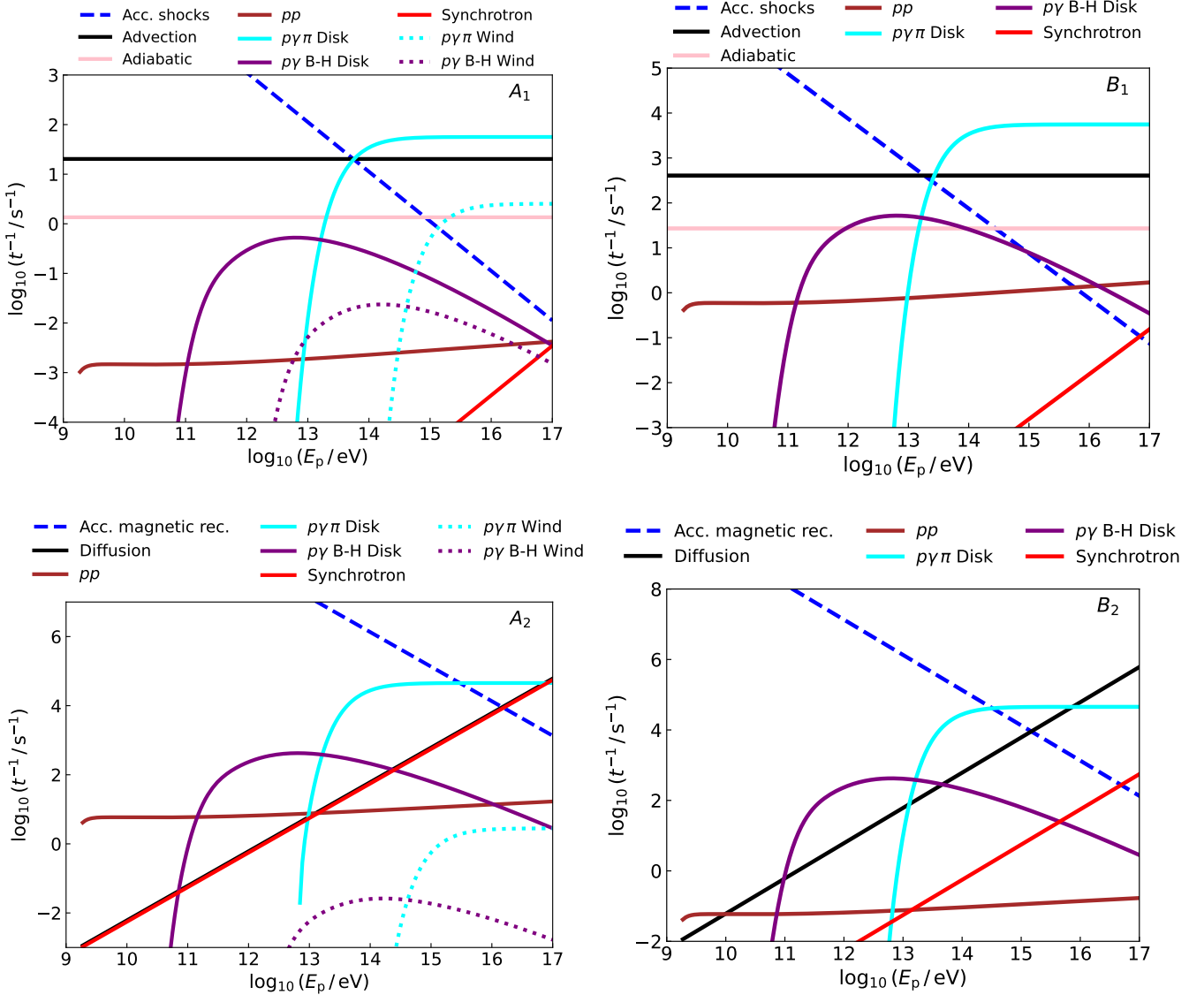


Figure 6: Timescales for acceleration, cooling, and escape of relativistic protons. Scenarios as in Fig. 5. **Top left:** Convective escape dominates up to ~ 20 TeV, beyond which photomeson production becomes the main energy loss channel. The maximum energy reached by protons is ~ 50 TeV. **Top right:** Escape is the dominant process, and the maximum energy is ~ 10 TeV. **Bottom left:** pp interactions dominate at low energies, up to ~ 100 GeV, followed by $p\gamma$ (photomeson) interactions at higher energies. The maximum energy is ~ 5 PeV. **Bottom right:** At low energies, pp interactions and diffusion dominate up to ~ 100 GeV; at higher energies, photo-hadronic losses prevail. The maximum proton energy is ~ 100 TeV.

5. Particle distribution and SEDs

We solve the transport equation to obtain the distribution of primary and secondary relativistic particles. The results for primary particles are shown in Figure 7, where we plot the distribution of primary electrons (left) and protons (right), for all scenarios. The distribution of secondary pairs produced via Bethe-Heitler mechanism is shown in Fig. 8. The number of relativistic secondary pairs exceeds that of primary electrons by several orders of magnitude. The maximum energies of the Bethe-Heitler pairs are approximately 20 GeV (A_1), 9 GeV (B_1), 1 TeV (A_2), and 200 GeV (B_2).

The next step is to calculate the SEDs of the various non-thermal processes. We refer to Romero and Vila (2008) and

references therein for the formulae used. Using the results presented in sections 3 and 4, we calculate the synchrotron and IC radiation for the primary electrons and secondary pairs, and the emission due to neutral pion decay produced by $p\gamma$ interactions.

Figure 9 shows the results for scenarios A_1 (left) and B_1 (right). Synchrotron and IC radiation from the secondary pairs are the dominant nonthermal processes, with maximum luminosities of $\sim 10^{34} \text{ erg s}^{-1}$ in scenario A_1 and $\sim 10^{36} \text{ erg s}^{-1}$ in scenario B_1 , around ~ 1 GeV. This emission dominates at energies of ~ 1 MeV, closely followed by IC radiation by primary electrons.

Figure 10 shows the SEDs of scenarios A_2 (left) and B_2 (right). In both cases, synchrotron and IC radiation from

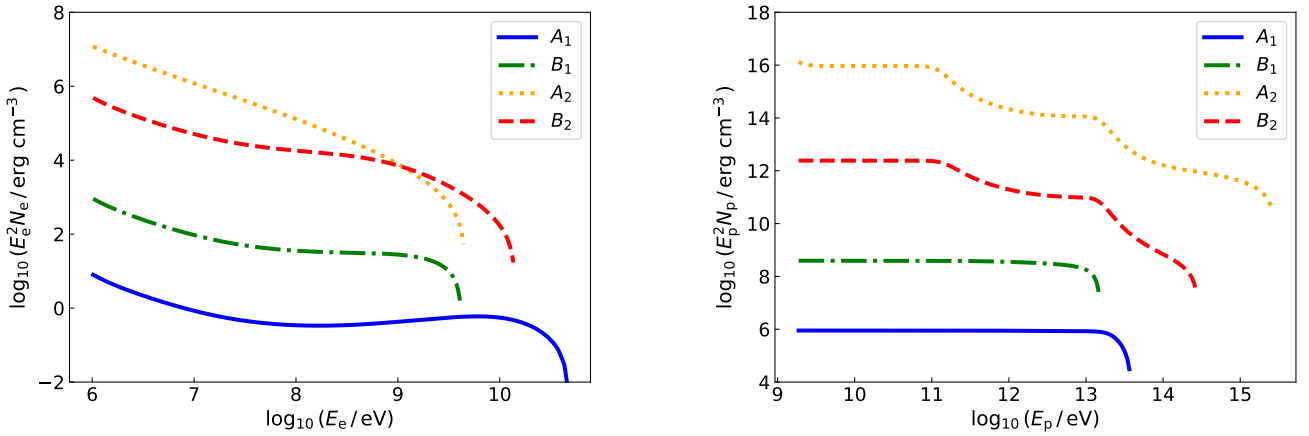


Figure 7: Distribution of primary relativistic particles for the various models. **Left:** Distribution of primary electrons. **Right:** Distribution of protons.

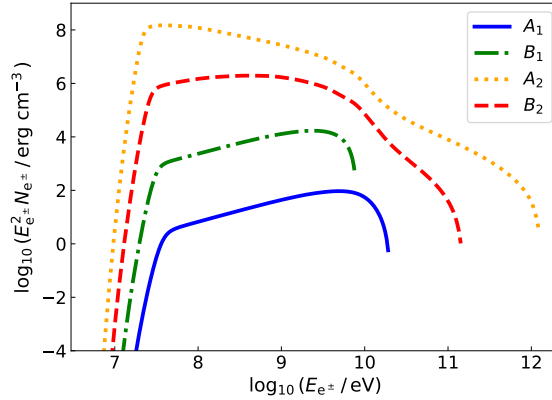


Figure 8: Distribution of secondary e^+ pairs produced via the Bethe-Heitler mechanism for all scenarios.

Bethe-Heitler secondary pairs are the dominant nonthermal processes. In scenario A_2 , synchrotron radiation from secondary pairs dominates the high-energy spectrum, with a maximum luminosity of approximately $10^{38} \text{ erg s}^{-1}$, and a cut-off around 5 GeV due to $\gamma\gamma$ annihilation. In scenario B_2 , the maximum luminosities of synchrotron and IC radiation from secondary pairs is $\sim 5 \times 10^{35} \text{ erg s}^{-1}$ around MeV and GeV. This emission surpasses that of the primary electrons across most of the energy range.

The absorption is calculated as in Cerutti et al. (2011). Absorption of nonthermal radiation produced by photon-photon annihilation is only relevant for energies higher than $\sim 10 \text{ GeV}$ (scenarios A_2 and B_2) and 100 GeV (scenarios A_1 and B_1). We consider the thermal radiation fields from the disk and the photosphere of the wind as targets of the nonthermal photons. We find that emission produced by the photomeson mechanism is completely suppressed.

We also show the thermal SEDs of the disk-driven wind and the disk (in the observer's frame). As expected, the radiation of the disk dominates the ULX emission, with its maximum in the

X-ray band, reaching apparent luminosities of $\sim 10^{40} \text{ erg s}^{-1}$ (A) and $\sim 10^{42} \text{ erg s}^{-1}$ (B).

We now apply our model to the source NGC 4190 ULX 1. This source has been classified as a hard ultraluminous due to the spectral hardness, which is consistent with a low inclination angle $i \approx 0$, indicating a face-on orientation (Ghosh and Rana, 2021; Abaroa et al., 2023; Combi et al., 2024).

Following Abaroa et al. (2023), we assume that the BH has a mass of $10 M_\odot$ and accretes matter from the donor star at a rate of $\dot{M} = 10 \dot{M}_{\text{Edd}}$. The fundamental disk parameters are the same as those listed in Table 1.

Figure 11 shows observational data from *NuSTAR* and *NICER* (from Combi et al. 2024) and the SEDs. Our model predicts the expected flux in the MeV–GeV range resulting from the interaction of secondary pairs with the magnetic field. In this energy range, the luminosity is $\sim 2 \times 10^{38} \text{ erg s}^{-1}$. We remark the change in the slope at $\sim 100 \text{ keV}$ due to the pair contribution. This feature can be used to test the presence of relativistic protons in the source through future observations by *COSI* satellite (Tomsick et al., 2023).

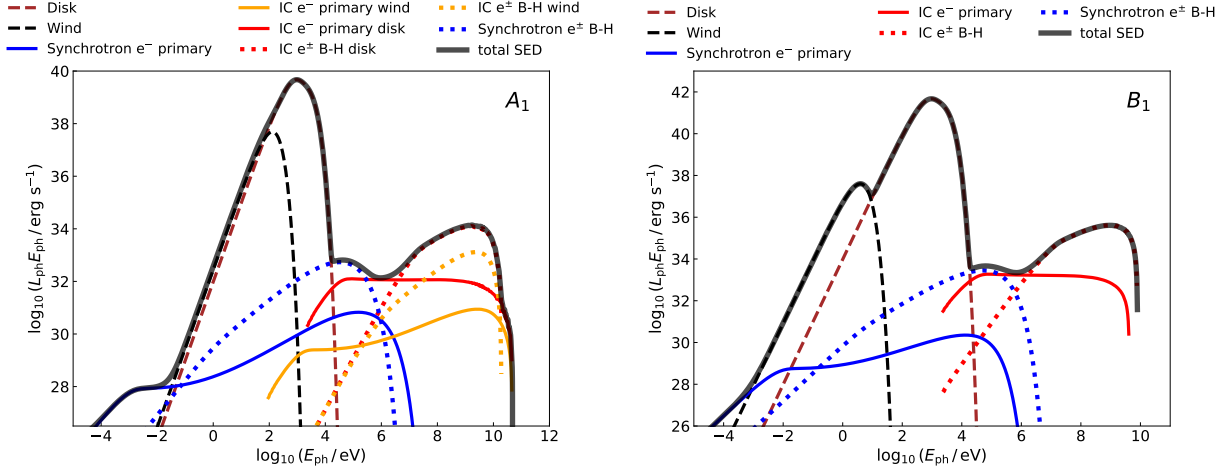


Figure 9: SEDs of the entire system for both accretion rates in the scenario of particle acceleration by diffusive shocks. Absorption effects are significant only above 100 GeV. The solid black line is the overall SED emission.

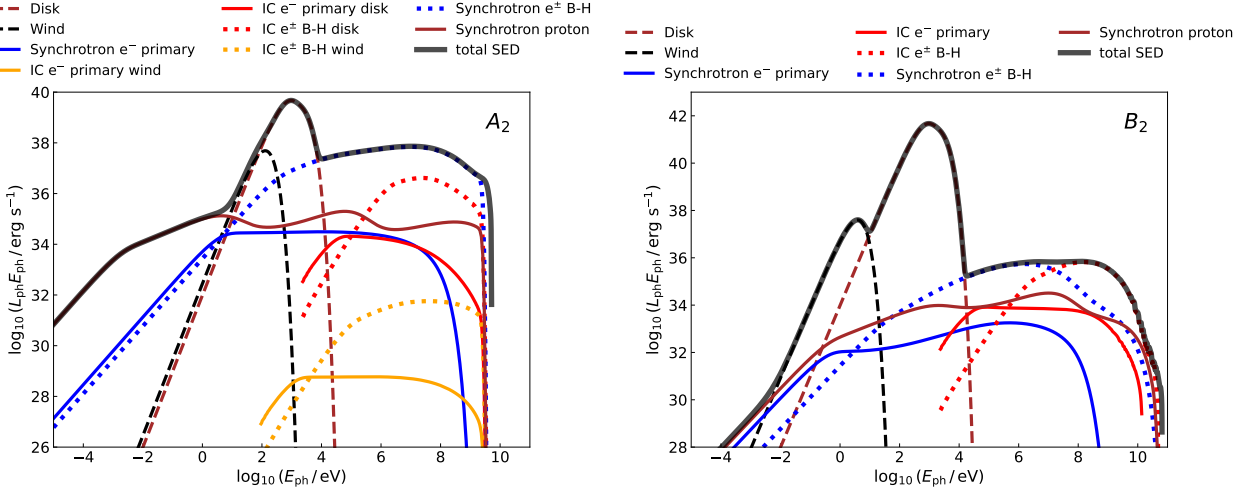


Figure 10: Similar to Fig. 9 but for the scenario of particle acceleration by magnetic reconnection.

6. Gamma-ray absorption in the wind

When the inclination angle of the system exceeds the semi-opening angle of the funnel ($i > \vartheta$), the radiation produced within the funnel is absorbed by the surrounding opaque wind. The gamma rays interact with the wind through Bethe-Heitler pair production and photomeson production: $\gamma + N \rightarrow N + e^- + e^+$ and $\gamma + N \rightarrow N + \pi^i$, where N represents a nucleon.

We assume that the wind is smooth and that it expands isotropically at a constant velocity, its density can be expressed as (Abaroa and Romero, 2024a):

$$\rho_w = \frac{\dot{M}_w}{4\pi r^2 v_w}, \quad (39)$$

where $\dot{M}_w \approx \dot{M}_{\text{input}}$ is the wind mass-loss rate, and r is the radial distance from the BH. The optical depth due to γ -nucleon interactions in the wind is given by Reynoso et al. (2008) as:

$$\tau_{\gamma N}(\vec{z}_j) = \int_0^\infty \sigma_{\gamma N} \left(\frac{\rho_w}{m_p} \right) d\rho_\gamma, \quad (40)$$

where $\sigma_{\gamma N} = \sigma_{\gamma N}^{\pi^i} + \sigma_{\gamma N}^{e^\pm}$ is the total cross section for γ -ray interactions with matter. The cross section parametrizations follow Maximon (1968) and Kelner and Aharonian (2008).

Figure 12 shows the gamma-ray flux for a galactic ULX located at 15 kpc and viewed at an inclination angle of $i = 45^\circ$, for scenarios A_1 and A_2 , both corresponding to mass accretion rates of $\dot{m} = 10$. A fraction of the gamma radiation is attenuated by the wind, and above 10 GeV, the absorption becomes total.

In scenarios with higher accretion rates, the wind becomes denser and can extend up to $\sim 2 \times 10^{12}$ cm, leading to complete suppression of radiation above ~ 1 MeV.

It is possible that some misaligned ULXs may exist within the Galaxy. These systems would remain undetected in X-rays due to wind obscuration, yet they could be observable in the MeV-GeV range if the accretion rates remain moderately super-

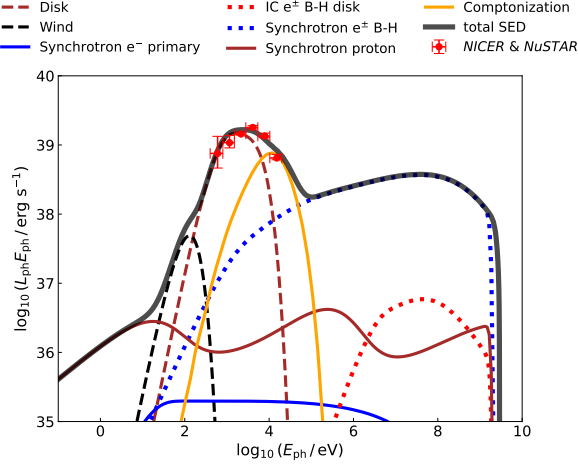


Figure 11: SED of the source NGC 4190 ULX-1, shown on a logarithmic scale. We show the thermal emission from the wind and innermost region of the accretion disk that escapes through the funnel, as well as non-thermal radiation produced by relativistic particles accelerated via magnetic reconnection. We add the inverse Compton SED from primary electrons accelerated far from the BH, following [Combi et al. \(2024\)](#). The red data points correspond to observations from *NICER* and *NuSTAR*. The solid black line is the total emission.

Eddington.

7. Discussion

The primary distinction between accretion scenarios *A* ($\dot{m}_{\text{input}} = 10$) and *B* ($\dot{m}_{\text{input}} = 10^3$) arise from properties that are highly sensitive to the accretion rate, such as the strength of the disk’s magnetic field, the semi-opening angle of the funnel (which narrows with increasing accretion rate), and the geometric and physical characteristics of the wind.

Key parameters governing the disk’s internal structure include the adiabatic index (γ), the advection parameter (f), the viscosity coefficient (α), and the degree of magnetization of the plasma (β). In our modeling, we adopted intermediate values for these quantities to provide a representative overview of the physical behavior of such systems. Nevertheless, variations in these parameters would affect essential quantities—most notably, the toroidal component of the magnetic field (B_ϕ)—and thereby influence the conditions in the particle acceleration region. The analytical framework presented here allows for straightforward recalculation under alternative assumptions, enabling researchers to explore a broader range of configurations. We consider the results reported in this work to be representative of the average behavior of these sources.

Another key factor is the location of the acceleration region for the nonthermal particle population. If this region lies farther from the BH, the disk radiation available for the Bethe-Heitler process diminishes significantly. As a result, the synchrotron emission from the resulting secondary pairs is also reduced. Moreover, the magnetic field typically decays with a toroidal profile beyond the Alfvén surface, which is generally located within $\sim 150 r_g$. As the field strength declines, both synchrotron losses and the particle acceleration rate decrease, leading to lower maximum energies for relativistic electrons and

protons. Although the precise location of internal shock formation remains uncertain, it is plausible that shocks arise from local perturbations induced by the surrounding wind once the outflow becomes compressible.

In scenarios *A*₁ and *B*₁, we computed the SEDs assuming the maximum gas injection rate (\dot{M}_{gas}) permitted within the funnel, thereby providing upper limits on the nonthermal radiation produced in these systems. However, under more realistic conditions, the actual number of particles entering the funnel is expected to be lower. Future multiwavelength observations—particularly in the X-ray and gamma-ray bands—could help to constrain the relevant parameter space by placing upper limits on the nonthermal luminosity, thereby providing indirect estimates of the power carried by relativistic particles, the funnel density, and the effective accretion rate. In addition, variability timescales and spectral slopes could offer clues about the location and efficiency of particle acceleration.

For scenarios *A*₂ and *B*₂, in which magnetic reconnection is the dominant acceleration mechanism, we adopted densities that yield an injected particle spectrum with index $p = 2$: specifically, $\rho_{A_2} = 0.1\rho_{\text{max}}$ and $\rho_{B_2} = 0.001\rho_{\text{max}}$. Deviations from these assumed densities would produce harder or softer particle spectra, significantly affecting the resulting emission. Thus, detailed spectral modeling and observational constraints will be essential for narrowing down the viable physical conditions in these sources.

This work does not explicitly model the mechanism by which matter is injected into the funnel. One plausible scenario involves the entrainment of hot plasma bubbles originating in the surrounding wind, which subsequently mix into the funnel region. Numerical simulations of supercritical accretion flows have shown that the accretion of complex, non-dipolar magnetic field configurations can lead to such outcomes by channeling gas into the polar regions of the BH ([McKinney and Blandford, 2009](#); [Romero, 2021](#)). These studies highlight the importance of magnetic field geometry in regulating mass loading and determining the internal structure of the funnel, which in turn influences the environment where particle acceleration occurs.

While such simulations provide valuable insights, they are limited by computational constraints and simplifying assumptions, particularly regarding radiative transfer and magnetic reconnection physics. Observational data, such as high-resolution imaging of jets and outflows or spectral signatures of entrained plasma, could help refine these models and provide empirical support for specific injection scenarios.

Our model predicts radiation emission in the largely unexplored energy range of 0.1–10 MeV from ULXs powered by BHs. In some extragalactic sources, such as NGC 4190 ULX-1, *NuSTAR* has detected emission up to energies of ~ 30 keV ([Combi et al., 2024](#)), which has been interpreted as IC upscattering of disk photons. Our model offers an alternative explanation based on the presence of relativistic protons. These two interpretations can be observationally distinguished, as the Bethe-Heitler mechanism produces a population of secondary pairs whose emission should extend well into the MeV regime. Consequently, high-sensitivity observations in the

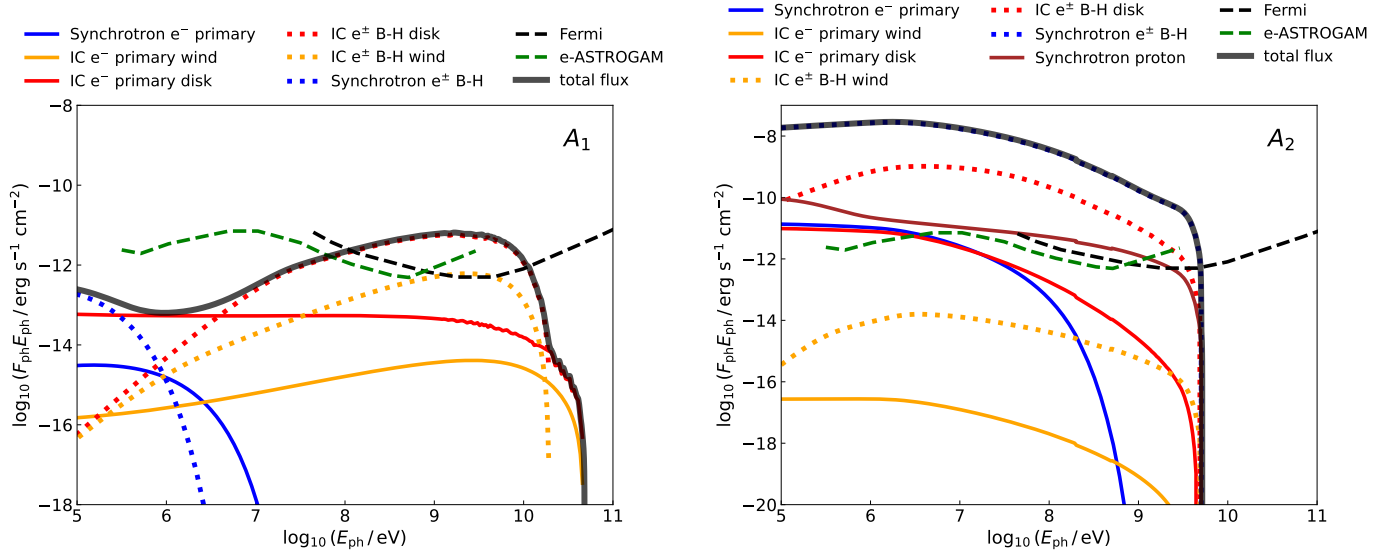


Figure 12: Predicted gamma-ray flux for a ULX with an inclination angle of $i = 45^\circ$ and a distance of $d = 15$ kpc. Sensitivities of the space-based telescopes *Fermi* and *e-ASTROGAM* are shown with dashed lines. The solid black line is the overall emission.

MeV band—which have not been possible since the decommissioning of *COMPTEL* on board the Compton Gamma Ray Observatory—are essential to probe the presence of relativistic protons in ULXs.

The proposed *e-ASTROGAM* mission (De Angelis et al., 2018), currently under consideration by the European Space Agency (ESA), is designed to explore the gamma-ray sky in the 0.3 MeV to 3 GeV range with unprecedented sensitivity and polarization capability. Its payload will include a silicon tracker to detect Compton scattering and pair production events, along with a calorimeter to measure the energy of the secondary particles. *e-ASTROGAM* has been proposed as the fifth medium-size (M5) mission in ESA’s Cosmic Vision program, with a potential launch date in 2029. Another highly relevant mission is *COSI* (the Compton Spectrometer and Imager) (Tomsick et al., 2014; Tomsick et al., 2023), scheduled for launch in 2027. *COSI* will operate in the 0.2–7 MeV band and is expected to provide critical observations to test scenarios involving hadronic components in ULXs.

Observations with next-generation MeV telescopes may also enable the detection of Galactic ULXs whose X-ray emission is heavily absorbed by the dense wind of the system when viewed at high inclination angles, while their softer gamma-ray emission—produced by secondary pairs—remains detectable. Since such misaligned systems are far more numerous than those viewed face-on, it is plausible that a significant population of obscured ULXs exists within our Galaxy. Their MeV radiation could serve as a key observational signature for their identification. Moreover, the model presented here could be tested in other super-Eddington accreting sources with jets, such as SS433 and Cyg X-3, where hadronic processes may also play a significant role in the high-energy emission.

8. Conclusions

We have investigated the consequences of relativistic proton injection into the funnels of ULXs powered by BHs. Our results show that protons can be accelerated to energies of ~ 10 –200 TeV and up to ~ 5 PeV, depending on the accretion scenario. These protons interact with thermal X-band photons from the disk via the Bethe-Heitler mechanism, producing secondary electron-positron pairs. The resulting pairs radiate primarily through synchrotron and IC processes, generating nonthermal emission that extends from ~ 1 MeV to ~ 10 GeV, with luminosities in the range of 10^{33} – 10^{38} erg s $^{-1}$.

We also find that photon-photon annihilation with the thermal radiation fields of the disk and wind does not significantly affect photons below ~ 10 GeV. However, it effectively suppresses the gamma-ray emission produced by neutral pion decay from photomeson interactions. This reinforces the role of Bethe-Heitler pair production as the dominant channel for high-energy radiation in these systems.

An important implication of our results is the potential for detecting obscured ULXs within the Galaxy. While X-ray emission can be heavily absorbed by the dense, radiation-driven wind, particularly in systems viewed at high inclination angles, the softer gamma-ray radiation from secondary pairs may still escape and be detectable. This opens a promising avenue for identifying hidden populations of ULXs through their MeV emission. Although no current missions operate in this critical energy range, upcoming instruments such as *e-ASTROGAM* and *COSI* are well suited to search for this predicted component in nearby sources. Additionally, *NuSTAR* observations in the tens-of-keV band could help identify candidate sources by revealing power-law spectra without an exponential cutoff, which may point to hadronic activity.

Finally, we emphasize that relativistic protons can produce high-energy signatures in BH binaries even in the absence of

jets. The detection of such spectral features in the MeV band remains a major observational challenge, but it offers a compelling opportunity to probe the presence of hadronic processes and the physical conditions in supercritical accretion flows.

Acknowledgements

This research was funded by PID2022-136828NB-C41/AEI/10.13039/501100011033/ and through the “Unit of Excellence María de Maeztu 2020-2023” award to the Institute of Cosmos Sciences (CEX2019-000918-M). LA thanks the Universidad Nacional de La Plata. Additional support came from PIP 0554 (CONICET).

References

- Abaroa, L., Romero, G.E., 2024a. Electromagnetic signatures of black hole clusters in the center of super-Eddington galaxies. *A&A* 691, A73. doi:[10.1051/0004-6361/202451903](https://doi.org/10.1051/0004-6361/202451903), [arXiv:2409.06787](https://arxiv.org/abs/2409.06787).
- Abaroa, L., Romero, G.E., 2024b. Super Winds and Radio Emission in X-ray Binary Systems. *RMAA Conf. Ser.* 56, 39–44. doi:[10.22201/ia.14052059p.2024.56.04](https://doi.org/10.22201/ia.14052059p.2024.56.04), [arXiv:2311.15050](https://arxiv.org/abs/2311.15050).
- Abaroa, L., Romero, G.E., Mancuso, G.C., Rizzo, F.N., 2024. The remarkable microquasar S26: A super-Eddington PeVatron. *A&A* 691, A93. doi:[10.1051/0004-6361/202450202](https://doi.org/10.1051/0004-6361/202450202), [arXiv:2409.16315](https://arxiv.org/abs/2409.16315).
- Abaroa, L., Romero, G.E., Sotomayor, P., 2023. Supercritical colliding wind binaries. *A&A* 671, A9. doi:[10.1051/0004-6361/202245285](https://doi.org/10.1051/0004-6361/202245285), [arXiv:2301.08635](https://arxiv.org/abs/2301.08635).
- Abramowicz, M.A., Calvani, M., Nobili, L., 1980. Thick accretion disks with super-Eddington luminosities. *ApJ* 242, 772–788.
- Abramowicz, M.A., Czerny, B., Lasota, J.P., Szuszkiewicz, E., 1988. Slim Accretion Disks. *ApJ* 332, 646.
- Aharonian, F.A., 2004. Very high energy cosmic gamma radiation: a crucial window on the extreme Universe.
- Akizuki, C., Fukue, J., 2006. Self-Similar Solutions for ADAF with Toroidal Magnetic Fields. *PASJ* 58, 469–475.
- Begelman, M.C., 1978. Black holes in radiation-dominated gas: an analogue of the Bondi accretion problem. *MNRAS* 184, 53–67.
- Begelman, M.C., Rudak, B., Sikora, M., 1990. Consequences of Relativistic Proton Injection in Active Galactic Nuclei. *ApJ* 362, 38.
- Berezinskii, V.S., Bulanov, S.V., Dogiel, V.A., Ptuskin, V.S., 1990. Astrophysics of cosmic rays.
- Bethe, H., Heitler, W., 1934. On the stopping of fast particles and on the creation of positive electrons. *Proceedings of the Royal Society of London. Series A, Containing Papers of a Mathematical and Physical Character* 146, 83–112.
- Bisnovatyi-Kogan, G.S., Blinnikov, S.I., 1976. A hot corona around a black-hole accretion disk as a model for CYG X-1. *Soviet Astronomy Letters* 2, 191–193. [arXiv:astro-ph/0003275](https://arxiv.org/abs/astro-ph/0003275).
- Blumenthal, G.R., Gould, R.J., 1970. Bremsstrahlung, Synchrotron Radiation, and Compton Scattering of High-Energy Electrons Traversing Dilute Gases. *Reviews of Modern Physics* 42, 237–271.
- Bosch-Ramon, V., Romero, G.E., Paredes, J.M., 2006. A broadband leptonic model for gamma-ray emitting microquasars. *A&A* 447, 263–276.
- Cerutti, B., Dubus, G., Malzac, J., Szostek, A., Belmont, R., Zdziarski, A.A., Henri, G., 2011. Absorption of high-energy gamma rays in Cygnus X-3. *A&A* 529, A120. doi:[10.1051/0004-6361/201116581](https://doi.org/10.1051/0004-6361/201116581), [arXiv:1103.3875](https://arxiv.org/abs/1103.3875).
- Chodorowski, M.J., Zdziarski, A.A., Sikora, M., 1992. Reaction Rate and Energy-Loss Rate for Photopair Production by Relativistic Nuclei. *ApJ* 400, 181.
- Combi, J.A., Fogantini, F.A., Saavedra, E.A., Romero, G.E., Abaroa, L., García, F., Luque-Escamilla, P., Martí, J., Cruz-Sanchez, N., 2024. Simultaneous NICER and NuSTAR observations of the ultraluminous source NGC 4190 ULX-1. *A&A* 686, A121. doi:[10.1051/0004-6361/202348895](https://doi.org/10.1051/0004-6361/202348895), [arXiv:2403.12300](https://arxiv.org/abs/2403.12300).
- Cruz-Sanchez, N., Fogantini, F.A., Saavedra, E.A., Abaroa, L., García, F., Combi, J.A., Romero, G.E., 2025. A broadband X-ray view of the ultraluminous sources in the galaxies ESO 501–023 and IC 5052. *A&A* 693, A122. doi:[10.1051/0004-6361/202452187](https://doi.org/10.1051/0004-6361/202452187).
- De Angelis, A., Tatischeff, V., Grenier, I., McEnery, J., Mallamaci, M., Tavani, M., Oberlack, U., Hanlon, L., Walter, R., Argan, A., Von Ballmoos, P., Bulgarelli, A., Bykov, A., Hernanz, M., Kanbach, G., Kuvvetli, I., Pearce, M., Zdziarski, A., Conrad, J., Ghisellini, G., Harding, A., Isern, J., Leising, M., Longo, F., Madejski, G., Martinez, M., Mazziotta, M., Paredes, J., Pohl, M., Rando, R., Razzano, M., Aboudan, A., Ackermann, M., Addazi, A., Ajello, M., Albertus, C., Álvarez, J., Ambrosi, G., Antón, S., Antonelli, L., Babic, A., Baibussinov, B., Balbo, M., Baldini, L., Balman, S., Bambi, C., Barres de Almeida, U., Barrio, J., Bartels, R., Bastieri, D., Bednarek, W., Bernard, D., Bernardini, E., Bernasconi, T., Bertucci, B., Biland, A., Bissaldi, E., Boettcher, M., Bonvicini, V., Bosch-Ramon, V., Bottacini, E., Bozhilov, V., Bretz, T., Branchesi, M., Brdar, V., Bringmann, T., Brogna, A., Budtz Jørgensen, C., Busetto, G., Buson, S., Busso, M., Caccianiga, A., Camera, S., Campana, R., Caraveo, P., Cardillo, M., Carlson, P., Celestin, S., Cermeño, M., Chen, A., Cheung, C., Churazov, E., Ciprini, S., Coc, A., Colafrancesco, S., Coleiro, A., Collmar, W., Coppi, P., Curado da Silva, R., Cutini, S., D’Ammando, F., De Lotto, B., de Martino, D., De Rosa, A., Del Santo, M., Delgado, L., Diehl, R., Dietrich, S., Dolgov, A., Domínguez, A., Dominis Prestre, D., Donnarumma, I., Dorner, D., Doro, M., Dutra, M., Elsaesser, D., Fabrizio, M., Fernández-Barral, A., Fioretti, V., Foffano, L., Formato, V., Fornengo, N., Foschini, L., Franceschini, A., Frackowiak, A., Funk, S., Fuschino, F., Gaggero, D., Galanti, G., Gargano, F., Gasparri, D., Gehrz, R., Giammaria, P., Giglietto, N., Giommi, P., Giordano, F., Giroletti, M., Ghirlanda, G., Godinovic, N., Gouiffés, C., Grove, J., Hamadache, C., Hartmann, D., Hayashida, M., Hryczuk, A., Jean, P., Johnson, T., José, J., Kaufmann, S., Khelifi, B., Kiener, J., Knödseder, J., Kole, M., Kopp, J., Kozhuharov, V., Labanti, C., Lalkovski, S., Laurent, P., Limousin, O., Linares, M., Lindfors, E., Lindner, M., Liu, J., Lombardi, S., Loparco, F., López-Coto, R., López Moya, M., Lott, B., Lubrano, P., Malyshev, D., Mankuzhiyil, N., Mannheim, K., Marchã, M., Marciánò, A., Marcote, B., Mariotti, M., Marisaldi, M., McBreen, S., Mereghetti, S., Merle, A., Mignani, R., Minervini, G., Moiseev, A., Morselli, A., Moura, F., Nakazawa, K., Nava, L., Nieto, D., Orienti, M., Orío, M., Orlando, E., Orleanski, P., Paiano, S., Paoletti, R., Papitto, A., Pasquato, M., Patricelli, B., Pérez-García, M., Persic, M., Piano, G., Pichel, A., Pimenta, M., Pittori, C., Porter, T., Poutanen, J., Prandini, E., Prantzos, N., Produit, N., Profumo, S., Queiroz, F., Rainó, S., Raklev, A., Regis, M., Reichardt, I., Rephaeli, Y., Rico, J., Rodejohann, W., Rodríguez Fernández, G., Roncadelli, M., Roso, L., Rovero, A., Ruffini, R., Sala, G., Sánchez-Conde, M., Santangelo, A., Saz Parkinson, P., Sbarrato, T., Shearer, A., Shellard, R., Short, K., Siegert, T., Siqueira, C., Spinelli, P., Stamerra, A., Starrfield, S., Strong, A., Strümke, I., Tavecchio, F., Taverna, R., Terzić, T., Thompson, D., Tibolla, O., Torres, D., Turolla, R., Ulyanov, A., Ursi, A., Vacchi, A., Van den Abeele, J., Vankova-Kirilovai, G., Venter, C., Verrecchia, F., Vincent, P., Wang, X., Weniger, C., Wu, X., Zaharijaš, G., Zampieri, L., Zane, S., Zimmer, S., Zoglauer, A., 2018. Science with e-astrogam: A space mission for mev–gev gamma-ray astrophysics. *Journal of High Energy Astrophysics* 19, 1–106. URL: <https://www.sciencedirect.com/science/article/pii/S2214404818300168>, doi:<https://doi.org/10.1016/j.jheap.2018.07.001>.
- del Valle, M.V., Romero, G.E., Luque-Escamilla, P.L., Martí, J., Ramón Sánchez-Sutil, J., 2011. Are T Tauri Stars Gamma-Ray Emitters? *ApJ* 738, 115. doi:[10.1088/0004-637X/738/1/115](https://doi.org/10.1088/0004-637X/738/1/115), [arXiv:1107.0645](https://arxiv.org/abs/1107.0645).
- Drury, L.O., 1983. REVIEW ARTICLE: An introduction to the theory of diffusive shock acceleration of energetic particles in tenuous plasmas. *Reports on Progress in Physics* 46, 973–1027.
- Eggum, G.E., Coroniti, F.V., Katz, J.I., 1985. Jet production in super-Eddington accretion disks. *ApJL* 298, L41–L45.
- Fabrika, S.N., Atapin, K.E., Vinokurov, A.S., Sholukhova, O.N., 2021. Ultraluminous X-Ray Sources. *Astrophysical Bulletin* 76, 6–38. doi:[10.1134/S1990341321010077](https://doi.org/10.1134/S1990341321010077), [arXiv:2105.10537](https://arxiv.org/abs/2105.10537).
- Fukue, J., 2004. Critical Accretion Disk. *PASJ* 56, 569–580.
- Fukue, J., 2005. Terminal Speed of On-Axis Jets from a Supercritical Accretion Disk. *PASJ* 57, 691–698.
- Fukue, J., Iino, E., 2010. Observational Appearance and Spectrum of Black-Hole Winds. *PASJ* 62, 1399.
- Ghosh, T., Rana, V., 2021. Super-Eddington accretion on to a stellar mass

- ultraluminous X-ray source NGC 4190 ULX1. *MNRAS* 504, 974–982. doi:[10.1093/mnras/stab774](https://doi.org/10.1093/mnras/stab774), [arXiv:2103.10265](https://arxiv.org/abs/2103.10265).
- Ginzburg, V.L., Syrovatskii, S.I., 1964. The Origin of Cosmic Rays.
- Ichimaru, S., 1977. Bimodal behavior of accretion disks: theory and application to Cygnus X-1 transitions. *ApJ* 214, 840–855. doi:[10.1086/155314](https://doi.org/10.1086/155314).
- Jaroszynski, M., Abramowicz, M.A., Paczynski, B., 1980. Supercritical accretion disks around black holes. *Acta Astron.* 30, 1–34.
- Justham, S., Rappaport, S., Podsiadlowski, P., 2006. Magnetic braking of Ap/Bp stars: application to compact black-hole X-ray binaries. *MNRAS* 366, 1415–1423. doi:[10.1111/j.1365-2966.2005.09907.x](https://doi.org/10.1111/j.1365-2966.2005.09907.x), [arXiv:astro-ph/0511760](https://arxiv.org/abs/astro-ph/0511760).
- Kagan, D., Sironi, L., Cerutti, B., Giannios, D., 2015. Relativistic Magnetic Reconnection in Pair Plasmas and Its Astrophysical Applications. *Space Sci. Rev.* 191, 545–573. doi:[10.1007/s11214-014-0132-9](https://doi.org/10.1007/s11214-014-0132-9), [arXiv:1412.2451](https://arxiv.org/abs/1412.2451).
- Kelner, S.R., Aharonian, F.A., 2008. Energy spectra of gamma rays, electrons, and neutrinos produced at interactions of relativistic protons with low energy radiation. *Phys. Rev. D* 78, 034013.
- Kelner, S.R., Aharonian, F.A., Bugayov, V.V., 2006. Energy spectra of gamma rays, electrons, and neutrinos produced at proton-proton interactions in the very high energy regime. *Phys. Rev. D* 74, 034018.
- Khangulyan, D., Hnatic, S., Aharonian, F., Bogovalov, S., 2007. TeV light curve of PSR B1259-63/SS2883. *MNRAS* 380, 320–330.
- King, A., 2008. Hyperaccretion. *New Astron. Rev.* 51, 775–777. doi:[10.1016/j.newar.2008.03.005](https://doi.org/10.1016/j.newar.2008.03.005).
- King, A.R., 2010. Black hole outflows. *MNRAS* 402, 1516–1522. doi:[10.1111/j.1365-2966.2009.16013.x](https://doi.org/10.1111/j.1365-2966.2009.16013.x), [arXiv:0911.1639](https://arxiv.org/abs/0911.1639).
- Kitaki, T., Mineshige, S., Ohsuga, K., Kawashima, T., 2021. The origins and impact of outflow from super-Eddington flow. *PASJ* 73, 450–466. doi:[10.1093/pasj/psab011](https://doi.org/10.1093/pasj/psab011), [arXiv:2101.11028](https://arxiv.org/abs/2101.11028).
- Kosec, P., Pinto, C., Walton, D.J., Fabian, A.C., Bachetti, M., Brightman, M., Fürst, F., Grefenstette, B.W., 2018. Evidence for a variable Ultrafast Outflow in the newly discovered Ultraluminous Pulsar NGC 300 ULX-1. *MNRAS* 479, 3978–3986. doi:[10.1093/mnras/sty1626](https://doi.org/10.1093/mnras/sty1626), [arXiv:1803.02367](https://arxiv.org/abs/1803.02367).
- Liang, E.P.T., Price, R.H., 1977. Accretion disk coronae and Cygnus X-1. *ApJ* 218, 247–252. doi:[10.1086/155677](https://doi.org/10.1086/155677).
- Lipunova, G.V., 1999. Supercritical disk accretion with mass loss. *Astronomy Letters* 25, 508–517.
- Liska, M., Hesp, C., Tchekhovskoy, A., Ingram, A., van der Klis, M., Markoff, S., 2018. Formation of precessing jets by tilted black hole discs in 3D general relativistic MHD simulations. *MNRAS* 474, L81–L85.
- Mastichiadis, A., Protheroe, R.J., Kirk, J.G., 2005. Spectral and temporal signatures of ultrarelativistic protons in compact sources. I. Effects of Bethe-Heitler pair production. *A&A* 433, 765–776.
- Maximon, L.C., 1968. Simple analytic expressions for the total born approximation cross section for pair production in a coulomb field. *J. Res. Nat. Bur. Stand., B* 72: 79–88(Jan.-Mar. 1968). URL: <https://www.osti.gov/biblio/4503338>, doi:[10.6028/jres.072B.011](https://doi.org/10.6028/jres.072B.011).
- McKinney, J.C., Blandford, R.D., 2009. Stability of relativistic jets from rotating, accreting black holes via fully three-dimensional magnetohydrodynamic simulations. *MNRAS* 394, L126–L130. doi:[10.1111/j.1745-3933.2009.00625.x](https://doi.org/10.1111/j.1745-3933.2009.00625.x), [arXiv:0812.1060](https://arxiv.org/abs/0812.1060).
- McKinney, J.C., Dai, L., Avara, M.J., 2015. Efficiency of super-Eddington magnetically-arrested accretion. *MNRAS* 454, L6–L10. doi:[10.1093/mnrasl/slv115](https://doi.org/10.1093/mnrasl/slv115), [arXiv:1508.02433](https://arxiv.org/abs/1508.02433).
- McKinney, J.C., Tchekhovskoy, A., Blandford, R.D., 2012. General relativistic magnetohydrodynamic simulations of magnetically choked accretion flows around black holes. *MNRAS* 423, 3083–3117. doi:[10.1111/j.1365-2966.2012.21074.x](https://doi.org/10.1111/j.1365-2966.2012.21074.x), [arXiv:1201.4163](https://arxiv.org/abs/1201.4163).
- Meier, D.L., 1979. The structure and appearance of winds from supercritical accretion disks. I. Numerical models. *ApJ* 233, 664–684.
- Mücke, A., Engel, R., Rachen, J.P., Protheroe, R.J., Stanev, T., 2000. Monte Carlo simulations of photohadronic processes in astrophysics. *Computer Physics Communications* 124, 290–314. doi:[10.1016/S0010-4655\(99\)00446-4](https://doi.org/10.1016/S0010-4655(99)00446-4), [arXiv:astro-ph/9903478](https://arxiv.org/abs/astro-ph/9903478).
- Narayan, R., Igumenshchev, I.V., Abramowicz, M.A., 2003. Magnetically Arrested Disk: an Energetically Efficient Accretion Flow. *PASJ* 55, L69–L72.
- Narayan, R., Yi, I., 1994. Advection-dominated Accretion: A Self-similar Solution. *ApJL* 428, L13.
- Ohsuga, K., Mineshige, S., Watarai, K.y., 2003. Spectral Energy Distribution in Supercritical Disk Accretion Flows through Photon-trapping Effects. *ApJ* 596, 429–436.
- Ohsuga, K., Mori, M., Nakamoto, T., Mineshige, S., 2005. Supercritical Accretion Flows around Black Holes: Two-dimensional, Radiation Pressure-dominated Disks with Photon Trapping. *ApJ* 628, 368–381.
- Okuda, T., Teresi, V., Toscano, E., Molteni, D., 2005. Black hole accretion discs and jets at super-Eddington luminosity. *MNRAS* 357, 295–303.
- Paczynski, B., Wiita, P.J., 1980. Thick accretion disks and supercritical luminosities. *A&A* 500, 203–211.
- Pinto, C., Middleton, M.J., Fabian, A.C., 2016. Resolved atomic lines reveal outflows in two ultraluminous X-ray sources. *Nature* 533, 64–67. doi:[10.1038/nature17417](https://doi.org/10.1038/nature17417), [arXiv:1604.08593](https://arxiv.org/abs/1604.08593).
- Reynoso, M.M., Romero, G.E., Christiansen, H.R., 2008. Production of gamma rays and neutrinos in the dark jets of the microquasar SS433. *MNRAS* 387, 1745–1754. doi:[10.1111/j.1365-2966.2008.13364.x](https://doi.org/10.1111/j.1365-2966.2008.13364.x), [arXiv:0801.2903](https://arxiv.org/abs/0801.2903).
- Romero, G., Gutiérrez, E., 2020. The Origin of Matter at the Base of Relativistic Jets in Active Galactic Nuclei. *Universe* 6, 99.
- Romero, G.E., 2021. The content of astrophysical jets. *Astronomische Nachrichten* 342, 727–734. doi:[10.1002/asna.202113989](https://doi.org/10.1002/asna.202113989), [arXiv:2106.14346](https://arxiv.org/abs/2106.14346).
- Romero, G.E., Vila, G.S., 2008. The proton low-mass microquasar: high-energy emission. *A&A* 485, 623–631.
- Shakura, N.I., Sunyaev, R.A., 1973. Reprint of 1973A&A....24..337S. Black holes in binary systems. Observational appearance. *A&A* 500, 33–51.
- Sądowski, A., Narayan, R., 2015. Powerful radiative jets in supercritical accretion discs around non-spinning black holes. *MNRAS* 453, 3213–3221. doi:[10.1093/mnras/stv1802](https://doi.org/10.1093/mnras/stv1802), [arXiv:1503.00654](https://arxiv.org/abs/1503.00654).
- Sądowski, A., Narayan, R., McKinney, J.C., Tchekhovskoy, A., 2014. Numerical simulations of super-critical black hole accretion flows in general relativity. *MNRAS* 439, 503–520. doi:[10.1093/mnras/stt2479](https://doi.org/10.1093/mnras/stt2479), [arXiv:1311.5900](https://arxiv.org/abs/1311.5900).
- Sotomayor Checa, P., Romero, G.E., 2019. Model for Population III microquasars. *A&A* 629, A76.
- Tomsick, J., Jean, P., Chang, H.K., Boggs, S., Zoglauer, A., Von Ballmoos, P., Amman, M., Chiu, J.L., Chang, Y.H., Chou, Y., Kierans, C., Lin, C.H., Lowell, A., Shang, J.R., Tseng, C.H., Yang, C.Y., 2014. COSI: The Compton Spectrometer and Imager Science Program, in: 40th COSPAR Scientific Assembly, pp. PSB.1–14–14.
- Tomsick, J.A., Boggs, S.E., Zoglauer, A., Hartmann, D., Ajello, M., Burns, E., Fryer, C., Karwin, C., Kierans, C., Lowell, A., Malzac, J., Roberts, J., Saint-Hilaire, P., Shih, A., Siegert, T., Slesator, C., Takahashi, T., Tavecchio, F., Wulf, E., Beechert, J., Gulick, H., Joens, A., Lazar, H., Neights, E., Oliveros, J.C.M., Matsumoto, S., Melia, T., Yoneda, H., Amman, M., Bal, D., von Ballmoos, P., Bates, H., Böttcher, M., Bulgarelli, A., Cavazzuti, E., Chang, H.K., Chen, C., Chu, C.Y., Ciabattini, A., Costamante, L., Dreyer, L., Fioretti, V., Fenu, F., Gallego, S., Ghirlanda, G., Grove, E., Huang, C.Y., Jean, P., Khatiya, N., Knödseder, J., Krause, M., Leising, M., Lewis, T.R., Lommler, J.P., Marcotulli, L., Martinez-Castellanos, I., Mittal, S., Negro, M., Nussirat, S.A., Nakazawa, K., Oberlack, U., Palmore, D., Panebianco, G., Parmiggiani, N., Parsotan, T., Pike, S.N., Rogers, F., Schutte, H., Sheng, Y., Smale, A.P., Smith, J., Trigg, A., Venters, T., Watanabe, Y., Zhang, H., 2023. The compton spectrometer and imager. URL: <https://arxiv.org/abs/2308.12362>, [arXiv:2308.12362](https://arxiv.org/abs/2308.12362).
- Veledina, A., Muleri, F., Poutanen, J., Podgorný, J., Dovčiak, M., Capitanio, F., Churazov, E., De Rosa, A., Di Marco, A., Forsblom, S.V., Kaaret, P., Krawczynski, H., La Monaca, F., Loktev, V., Lutovinov, A.A., Molkov, S.V., Mushtukov, A.A., Ratheesh, A., Rodriguez Cavero, N., Steiner, J.F., Sunyaev, R.A., Tsygankov, S.S., Weisskopf, M.C., Zdziarski, A.A., Bianchi, S., Bright, J.S., Bursov, N., Costa, E., Egron, E., Garcia, J.A., Green, D.A., Gurwell, M., Ingram, A., Kajava, J.J.E., Kale, R., Kraus, A., Malyshev, D., Marin, F., Matt, G., McCollough, M., Mereminskiy, I.A., Nizhelsky, N., Pivano, G., Pilia, M., Pittori, C., Rao, R., Righini, S., Soffitta, P., Shevchenko, A., Svoboda, J., Tombesi, F., Trushkin, S.A., Tsybulev, P., Ursini, F., Wu, K., Agudo, I., Antonelli, L.A., Bachetti, M., Baldini, L., Baumgartner, W.H., Bellazzini, R., Bongiorno, S.D., Bonino, R., Brez, A., Bucciantini, N., Castellano, S., Cavazzuti, E., Chen, C.T., Ciprini, S., Del Monte, E., Di Gesu, L., Di Lalla, N., Donnarumma, I., Doroshenko, V., Ehler, S.R., Enoto, T., Evangelista, Y., Fabiani, S., Ferrazzoli, R., Gunji, S., Hayashida, K., Heyl, J., Iwakiri, W., Jorstad, S.G., Karas, V., Kislat, F., Kitaguchi, T., Kolodziejczak, J.J., Latronico, L., Liodakis, I., Maldera, S., Manfreda, A., Marinucci, A., Marscher, A.P., Marshall, H.L., Massaro, F., Mitsuishi, I.,

- Mizuno, T., Negro, M., Ng, C.Y., O'Dell, S.L., Omodei, N., Oppedisano, C., Papitto, A., Pavlov, G.G., Peirson, A.L., Perri, M., Pesce-Rollins, M., Petrucci, P.O., Possenti, A., Puccetti, S., Ramsey, B.D., Rankin, J., Roberts, O., Romani, R.W., Sgrò, C., Slane, P., Spandre, G., Swartz, D., Tamagawa, T., Tavecchio, F., Taverna, R., Tawara, Y., Tennant, A.F., Thomas, N.E., Trois, A., Turolla, R., Vink, J., Xie, F., Zane, S., 2024. Cygnus X-3 revealed as a Galactic ultraluminous X-ray source by IXPE. *Nature Astronomy* doi:[10.1038/s41550-024-02294-9](https://doi.org/10.1038/s41550-024-02294-9).
- Vieyro, F.L., Romero, G.E., 2012. Particle transport in magnetized media around black holes and associated radiation. *A&A* 542, A7. doi:[10.1051/0004-6361/201218886](https://doi.org/10.1051/0004-6361/201218886), [arXiv:1204.4469](https://arxiv.org/abs/1204.4469).